

# Discrete differential geometry of fluvial landscapes

Nathaniel Klema<sup>1,2</sup>, Leif Karlstrom<sup>2</sup>, and Joshua Roering<sup>2</sup>

<sup>1</sup>Department of Physics and Engineering, Fort Lewis College, Durango, Colorado 81301, U.S.A.

<sup>2</sup>Department of Earth Sciences, University of Oregon, Eugene, Oregon 97403, U.S.A

**Correspondence:** Nathaniel Klema (ntklema@fortlewis.edu)

**Abstract.** Geomorphology as a discipline is defined by the use of topographic form to understand surface processes on Earth and other planets. In practice this requires drawing connections between quantitative metrics of surface geometry and rates of exhumation, to understand the spatial partitioning of different erosion processes and the feedback between them. Curvature, perhaps the most fundamental way to measure and categorize surfaces of any kind, also appears explicitly in many erosion models and is therefore of significance to geomorphology. However, there is ambiguity in how curvature of discretely sampled topographic surfaces such as digital elevation models is defined and calculated. Many landscape evolution studies leverage curvature calculated as the scalar output of the Laplacian operator applied to map-view projections, which approximates but can deviate significantly from the surface curvature tensor at a point. In this study we use a formal surface theory approach to compute intrinsic and extrinsic curvature metrics, and associated shape-class distributions, of approximate steady-state fluvial topography of the Oregon Coast Range, USA. We develop a workflow, including careful spectral filtering to isolate wavelengths of interest, that provides a nuanced view of landscape geometry while simultaneously eliminating systematic errors arising from map-view approaches to topographic analysis. Two invariants of the curvature tensor – the mean and Gaussian curvatures – reveal systematic structure of topographic geometry in channel and ridge networks that appears to capture transitions between hillslope, debris flow, and fluvial process regimes. Mean curvature and associated shape classes are equipartitioned between concave-down and concave-up elements, forming complementary branching structures that span the landscape. These results suggest that formal surface theory approaches could prove valuable in maximizing the utility of digital elevation data through differentiation and definition of process regimes that drive the evolution of fluvial landscapes.

## 1 Introduction

The Earth's surface contains multi-scale signatures of the processes that have shaped it. Over length scales of  $10^2 - 10^4$  km, long-wavelength relief tracks patterns of lithospheric deformation and isostasy (Wieczorek, 2015) with relief generally increasing with the horizontal scale of measurement (Turcotte, 1987). The resulting gravitational gradients drive surface erosion that shapes the landscape at finer scales (Perron et al., 2008; Hooshyar et al., 2020; Bonetti et al., 2020) through a combination of diffusive (Roering et al., 2001a), advective (Whipple and Tucker, 1999), and stochastic mass transport (Furbish et al., 2009).

In the spirit of reductionism, geomorphic studies often focus on regions where a single erosion process is assumed dominant. There are many established approaches to partitioning the landscape into process domains (Montgomery and Foufoula-

Georgiou, 1993; Shary, 1995; Jasiewicz and Stepinski, 2013). However, compartmentalization comes at the risk of oversimplifying interactions between processes. For example, the transition from hillslopes to fluvial channels commonly occurs in topographic hollows where gullies begin to incise. Here, interactions between hillslope and fluvial processes influence both long-term landscape evolution (Perron et al., 2012) and short-term mass motions that are of interest for hazard prediction (Yanites et al., 2025; Struble et al., 2023). However, the complexity and variability of mass transport processes have limited the tools available for consistently quantifying geometry in this region. As another example, the transition from curved hilltops to linear hillslopes spans a geometric transition that requires accurate quantification of both slope and curvature with changing surface orientation (Roering et al., 1999). As digital elevation models (DEMs) become increasingly high resolution in space and multi-temporal (Crosby et al., 2020), there are growing opportunities to understand landscapes holistically using quantitative tools that are accurate, and informative, across all regions of the landscape.

The potential of differential geometry for DEM processing has already been established in several parallel earth science disciplines. Examples include models of topographic stresses relevant to critical zone processes (Moon et al., 2017), of sheet joint development on bedrock surfaces (Martel, 2011), and models that describe the structure of bedrock folds (Mynatt et al., 2007; Pearce et al., 2006). Topographic contour curvature has also been recognized as a key ingredient for scale-independent computation of flow accumulation and its role in landscape evolution models (Bonetti et al., 2018, 2020). However, widespread adoption of these techniques has been slow, perhaps because of a conceptual disconnect between resultant metrics of topographic geometry and area-space landscape partitioning frameworks that are at the core of landscape evolution theory.

With this in mind, here we develop a landscape classification workflow based on invariants of the curvature tensor. This provides a fully self-consistent means of calculating all common topographic metrics on discretely sampled DEMs and extracts surface curvature information with rich potential. This approach is robust against distortions that arise from derivative calculations on steep, complex surfaces (Bergbauer and Pollard, 2003; Minár et al., 2020), thus allowing for a curvature-based landscape partitioning approach that is continuous across all process transitions in a fluvial basin. We apply our method to topography of the Oregon Coast Range, long taken to be a type setting for near-steady-state landscape dynamics in which uplift is balanced by erosion in locations with characteristic ridge/valley topography.

## 50 1.1 The use of curvature in geomorphology

The connection between surface process rates and curvature was recognized as early as the late 19th century when work by G.K. Gilbert and W.M. Davis suggested connections between hillslope convexity and rates denudation in mountain terrains (Gilbert, 1877; Davis, 1892). Efforts to define topographic structure predate these observations, however. As has been pointed out in Bonetti et al. (2018), topographic curvature as been studied since at least the middle nineteenth century: Arthur Cayley (Cayley, 1859) used topographic contours to show that watershed bounding ridges are composed of “summits” (we will term these structures “domes”) connected by “knots” (we will call these “saddles”) such that each ridge line contains one more “summit” than “knot”. He argued that “immits” (we will call these “basins”) would be similarly connected by bridging saddle structures such that there is one more “immit” than connecting saddle. Prominent physicist James Clerk Maxwell (Maxwell, 1870)

similarly argued that the Earth’s surface could be sorted into four shape classes; “hills” (domes), “dales” (basins), “passes”  
60 connecting hills (antiformal saddles), and “bars” connecting dales (synformal saddles). Maxwell showed that continuity of the  
surface requires there to always be one more dale than bar, and one more hill than pass, thus reaching the same conclusion as  
Cayley and making a quantitative statement about the distribution of topographic curvatures.

Today, several curvature-based metrics are used in geomorphology for surface classification and as an ingredient in mechanistic  
transport laws. For examples of classification, Shary (1995) derived 12 curvature metrics which were used in a landscape par-  
65 titioning scheme, and Passalacqua et al. (2010) used geodesic curvature of topographic contours in combination with drainage  
area thresholding to extract channel networks from DEMs. Bonetti et al. (2018) showed that curvature is intimately connected  
to accumulation of overland flow, Minár et al. (2020) presented an extensive list of possible land surface curvature metrics and  
proposed possible links to topographic equilibrium, and Schmidt et al. (2003) derived curvature metrics using 2-d polynomial  
fits of topography for GIS applications. Such classification schemes have proven useful in surface process studies (Sofia, 2020)  
70 and for mapping topographic characteristics of hazard susceptibility (Luu et al., 2024) and land use (Riza et al., 2022).

In mechanistic erosion models curvature arises from continuity requirements as the divergence of a gradient driven sediment  
flux law (Culling, 1960; Fernandes and Dietrich, 1997). Curvature is thus often used as a quantitative proxy for spatial variation  
in erosion rates (Struble et al., 2024). For example, at the scale of orogenic provinces, simple models of landscape response to  
uplift model erosion with a heat equation where erosion rates are taken to be the product of long-wavelength surface curvature  
75 and an empirical diffusivity constant (Watts, 2001; Ruh, 2020). At finer spatial scales, curvature-driven diffusion of ridges  
(Roering et al., 1999; O’Hara et al., 2019) is overtaken by advective transport of sediment by concentrated overland flow  
within the fluvial network as drainage area increases (Whipple and Tucker, 1999), and channels themselves are defined on the  
basis of curvature (Passalacqua et al., 2010). Accounting for both of these processes and adding a source term to represent  
bedrock uplift, a commonly used form of the landscape evolution equation arises as

$$80 \quad \frac{\partial z}{\partial t} = U - KA^m |\nabla z|^n - D\nabla^2 z, \quad (1)$$

where  $z$  is surface elevation,  $U$  is uplift rate,  $A$  is drainage area upstream of a given point (a proxy for stream discharge), and  
 $K$ ,  $m$ ,  $n$ , and  $D$  are empirical constants that account for the geologic, hydrologic, and environmental factors that modulate  
rates of mass transport. The second term on the RHS is the ‘stream power’ model for fluvial erosion (Whipple and Tucker,  
1999), while the third term models linear hillslope diffusion. Steady state refers to the situation where  $dz/dt = 0$ , in which  
85 case equation 1 can be rewritten as

$$U = KA^m |\nabla z|^n + D\nabla^2 z. \quad (2)$$

If the parameters  $K$ ,  $m$ ,  $n$ , and  $D$  in Eq. 2 are spatially and temporally constant, then variation in the geometric properties of a  
topographic surface (such as stream longitudinal gradient and hilltop curvature) maps variation in uplift rate  $U$  (Wobus et al.,  
2006). Conversely, in regions where uplift is uniform, geometric variation can be used to infer the effects of climatic, lithologic,  
90 and environmental factors on the rate and style of erosion (Ferrier et al., 2013; Stock and Montgomery, 1999; Amundson et al.,

2015). An extensive literature has been established leveraging one or both of these limits (Perron et al., 2009; Whipple et al., 2013).

We show that a formal differential geometry approach extracts geometric information from the curvature tensor directly, and can provide a self-consistent means of evaluating topographic form across process domains. Comparing invariants of the curvature tensor to upstream drainage area  $A$  at a point, a quantity assumed to underlie empirical scaling relations (Hack et al., 1957) and process regimes (Flint, 1974; Montgomery and Buffington, 1997; Kirby and Whipple, 2012) alike, provides an intuitive description of river basin development. This approach also makes a quantitative connection between the early landscape organization theories of Maxwell and Cayley and drainage area analysis methods common in fluvial geomorphology today.

## 100 2 Oregon Coast Range study site

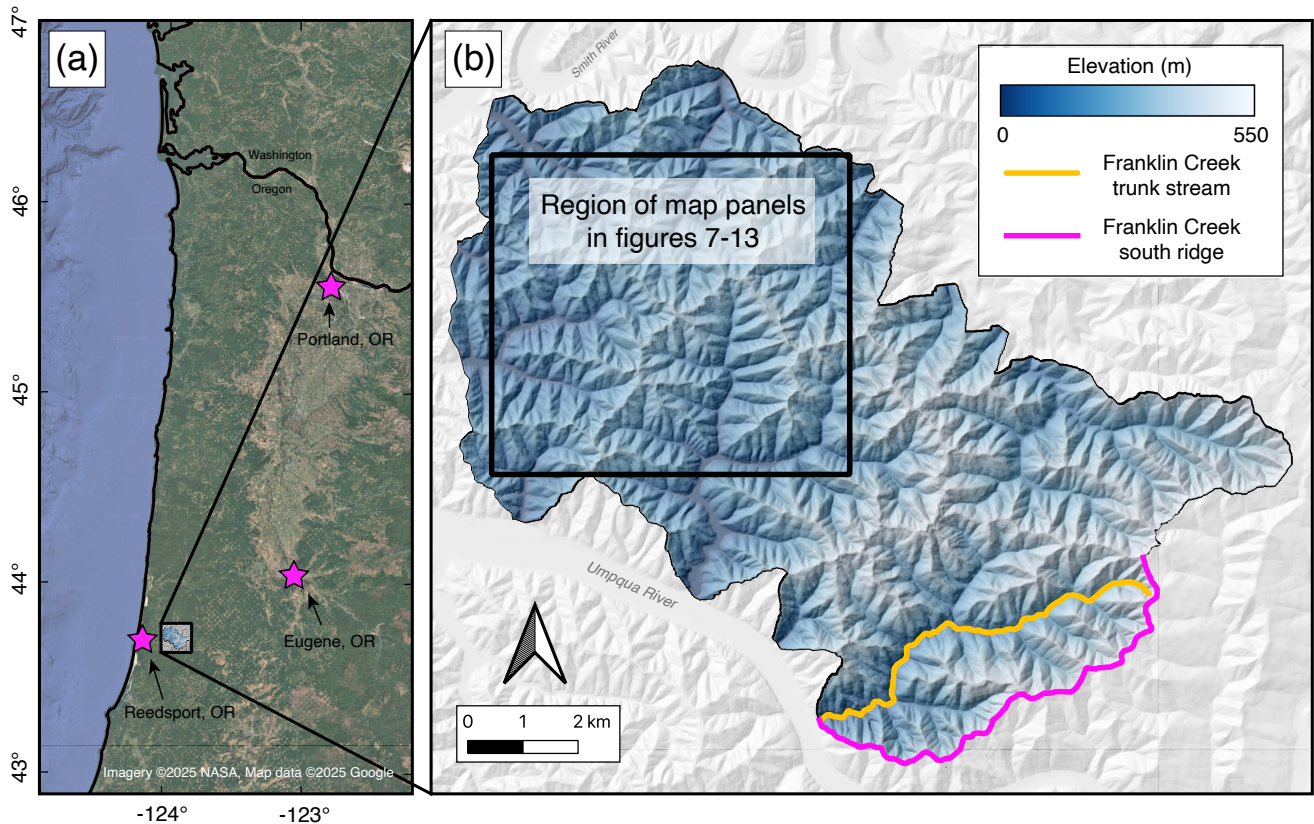
We test our method of geometric classification in the central Coast Range, USA, a forearc landscape of the Cascades subduction zone. Our study area is a suite of  $\sim 10 \text{ km}^2$  basins that host fluvial and debris flow channel networks between the Umpqua and Smith River basins near Reedsport, Oregon. Bedrock in this study area is composed entirely of the Tyee Formation (Baldwin, 1961; Beaulieu and Hughes, 1975), a 3 km thick suite of accreted Eocene turbidites that was subject to uplift during the Miocene (McNeill et al., 2000; Wells et al., 2014) and continues to be uplifted today with long-term rates ranging from  $0.05 \text{ mm yr}^{-1}$  to over  $0.4 \text{ mm yr}^{-1}$  (Kelsey et al., 1996; Personius, 1995).

The Coast Range has long been identified and studied as an archetypal steady-state landscape due to its uniform ridge-valley topography (Dietrich and Dunne, 1978; Montgomery, 2001), and documented correlations between drainage averaged erosion rates, uplift rates, and topographic proxies for erosion rate (Reneau and Dietrich, 1991; Heimsath et al., 2001; Struble et al., 2024). We focus on a small portion of the Coast Range without much variation in lithology (Baldwin, 1961; Beaulieu and Hughes, 1975) or climate (Daly and Bryant, 2013). Owing to the relatively gentle dip of the bedrock, this area is not subject to deep-seated landslides that interrupt characteristic ridge-valley terrain in other portions of the Coast Range (Roering et al., 2005; LaHusen et al., 2020).

## 3 Definitions of curvature

### 115 3.1 Intrinsic versus extrinsic curvatures

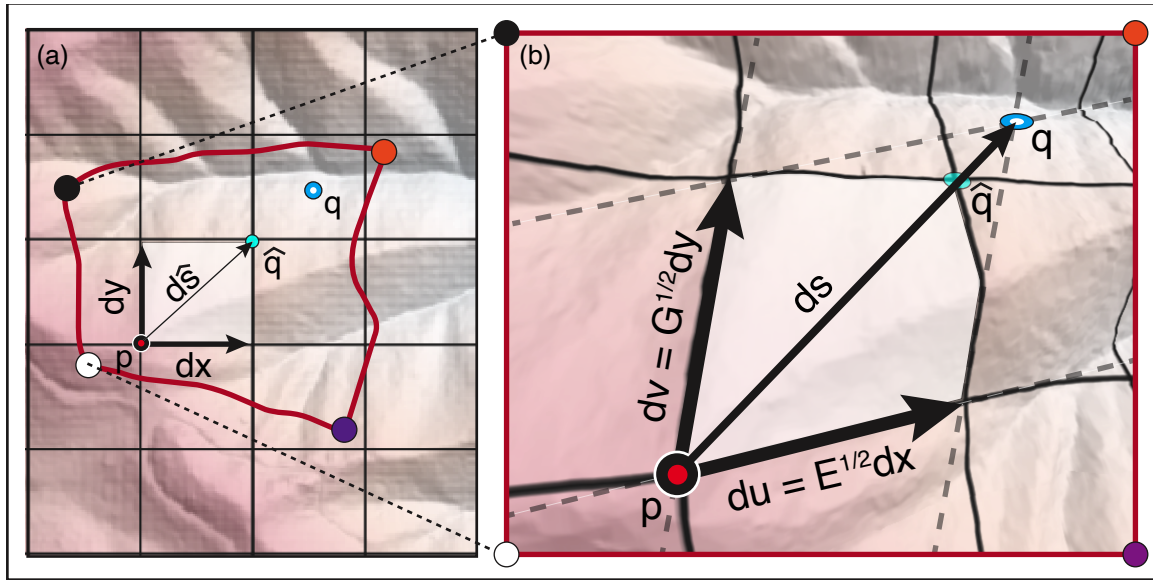
The term “curvature” formally refers to a class of mathematical operations that quantify deviations of a surface (or more generally, a manifold) from being planar (Needham, 2021). The tools of differential geometry and tensor calculus were in part developed to describe these operations (Pescic, 2007). There are several ways to define curvature, which can be classified as either ‘intrinsic’ or ‘extrinsic’. Intrinsic curvatures are independent of coordinate system and can be calculated using only local



**Figure 1. Map of study area. a.** Overview map of Cascadia coastal region showing location of study site. Satellite imagery from Google Earth, accessed through QGIS XYZ tiles on June 13th, 2025. **b.** Elevation map of study area showing location of the Franklin Creek trunk stream and southern ridge of Franklin Creek basin analyzed in Sect. 5.3. Black outline shows region of focused maps in figures 7-13

120 surface information (Needham, 2021). Extrinsic curvatures are built using external coordinates and so depend on the choice of  
 125 reference frame (Struik, 1950; O'Neill, 2006).

On discretely sampled landscape models (DEMs), the accurate calculation of either intrinsic or extrinsic curvatures requires  
 careful consideration of coordinates to avoid distortions that come from projection of topography onto a map grid. The effects  
 of projection can be seen in Fig. 2, which compares the distances and angles of a map projection (Fig. 2.a) to those of the same  
 125 grid lines overlaying the 3-D surface (Fig. 2.b). In the map-view representation, the E-W and N-S grid lines are perpendicular  
 and evenly spaced. If one were to define displacement vectors  $dx$  and  $dy$  emanating from point  $p$  along these grid lines, their  
 combination would create a resultant displacement  $d\hat{s}$  ending at point  $\hat{q}$ . In Fig. 2.b, however, displacement vectors  $du$  and  
 $dv$ , which connect  $p$  to the same points on the surface as  $dx$  and  $dy$  respectively, are not perpendicular and their combination  
 results in a displacement ( $ds$ ) that maps to a different point ( $q$ ). It can be seen that neighboring grid cells do not have uniform  
 130 dimensions, and that the angle between the grid lines is not consistent.



**Figure 2. Difference between distances and angles measured on a map projection versus on the surface. a.** Map projection of DEM including map grid defined by E-W and N-S lines with grid spacing  $dx$  and  $dy$ . The red line corresponds to the rectangular outline of panel b. **b.** DEM viewed as a 2-d manifold embedded in a 3-d space. Dashed lines show a locally defined  $uv$  coordinate system that follows  $x$  and  $y$  curves on the map projection, but which are not orthogonal or of equal length due to surface distortion.  $E$  and  $G$  are coefficients of the first fundamental form, and  $ds$  is the displacement vector that results moving one grid space along each of these coordinate vectors

Thus, accurate geometric calculations on topography require viewing a DEM not as a regular grid, but as a set of irregularly spaced data points sampling a surface, an approach that is similar in spirit to how elevation data are treated in landscape evolution models (Tucker et al., 2001). To accurately define a surface, distances and angles between grid cells are not treated as uniform quantities, as they result from calculations of surface variation about each point in a local reference frame. This specific problem of topographic projection was recognized by Leonard Euler in 1775 and motivated the work of Carl Frederick Gauss, who, roughly fifty years after Euler's observation, established the mathematical framework for accurate geometric classification of surfaces (Gauss, 1902; Needham, 2021). Using an approach similar to Gauss, we derive both intrinsic and extrinsic topographic curvature metrics built on invariant surface quantities.

### 140 3.2 Curvature invariants and related shape classes categories

As you change orientation about any point on a continuous surface, two perpendicular directions define the maximum and minimum normal curvature values (O'Neill, 2006). Between these directions, the curvature varies smoothly as

$$\kappa(\theta) = k_1 \cos^2 \theta + k_2 \sin^2 \theta, \quad (3)$$

where the extrema  $k_1$  and  $k_2$  are called the principal curvatures and  $\theta$  is an angular direction measured within the surface  
145 tangent plane. Equation 3, known as Euler's Theorem (not to be confused with the 'Euler's Theorem' in number theory or the  
'Euler Identity' of complex analysis), shows that the principal curvatures can be used to calculate normal curvature along any  
path over the surface. The principal curvatures are invariant quantities, meaning their values are independent of reference frame.

The principal curvature can be used to calculate two other useful invariant quantities that will be more central to our analysis;  
150 the 'mean' and 'Gaussian' curvatures. The mean curvature, and extrinsic quantity, follows directly from Euler's Theorem and  
is the value about which the curvature oscillates as a function of angle on the surface (Eq. 3). While it can be calculated as the  
average curvature of any two perpendicular paths, we define it in terms of the principal curvatures as

$$K_M = \frac{k_1 + k_2}{2}. \quad (4)$$

The Gaussian curvature ( $K_G$ ) can be defined as the product of the principal curvatures

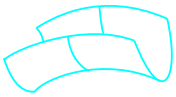

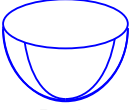


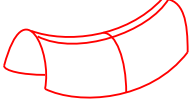

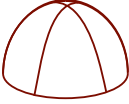
$$155 \quad K_G = k_1 k_2. \quad (5)$$

This value is intrinsic, meaning both that it is unchanged under isometric transformations, and that it does not depend on the  
actual shape of the surface in space. Instead  $K_G$  captures a more subtle quality: the degree of stretching or bending required to  
deform a flat plane so that it conforms to the surface (O'Neill, 2006). Note that the units of  $K_G$  ( $\text{m}^{-2}$ ) are not the same as  $K_M$   
( $\text{m}^{-1}$ ).

160 The mean and Gaussian curvatures together determine the geometry about a point uniquely as one of eight distinct shape  
classes (Bergbauer and Pollard (2003); Fig. 3). Since the Gaussian curvature is the product of the two principal curvatures, it  
will only be positive in instances where  $k_1$  and  $k_2$  have the same sign. Positive  $K_G$  thus correlates to either domes or basins,  
though we cannot discern which from  $K_G$  alone. If  $K_G$  is negative, then  $k_1$  and  $k_2$  have opposing signs and the surface is  
locally a saddle. Again, the orientation in space cannot be determined from this intrinsic quality.

165 In cases where either  $k_1$  or  $k_2$  is equal to zero,  $K_G$  is also zero. Such shapes comprise a class of 'developable surfaces', which  
are intrinsically flat and can be formed from a plane without altering surface area. 'Relatively developable surfaces' can be  
extracted from the landscape by assigning a zero value to curvatures under a defined threshold (Mynatt et al., 2007). Curvature  
thresholding to extract developable forms is a promising approach for classifying landforms. However, we do not explore this  
further here.

170 The orientation of a shape is an extrinsic quality that can be determined from the mean curvature, allowing us to put geometric  
classifications based on  $K_G$  into a landscape reference frame.  $K_M$  is positive in two cases: when both  $k_1$  and  $k_2$  are positive,  
or when the higher-magnitude curvature ( $k_1$ ) is positive. This means that points in the landscape with  $K_M > 0$  are concave  
down and are locally either domes or antiformal saddles. Similarly, if  $K_M$  is negative, then the surface must be mostly concave  
up and is either a basin or synformal saddle. More generally, the sign of the mean curvature allows us to differentiate between  
175 the divergence and convergence of surface gradient vectors.

	$K_G < 0$	$K_G = 0$	$K_G > 0$
$K_M < 0$	 Synformal Saddle	 Synform	 Basin
$K_M = 0$	 Perfect Saddle	 Plane	
$K_M > 0$	 Antiformal Saddle	 Antiform	 Dome

**Figure 3. Shape classes into which points on the surface can be sorted based on the signs on the Mean ( $K_M$ ) and Gaussian ( $K_G$ ) curvatures.** In this analysis we focus on those classes that can be assigned based on raw curvature values, which are synformal saddles, antiformal saddles, basins, and domes, and do not include developable surfaces or perfect saddles. Modified from Mynatt et al. (2007)

In cases where  $k_1$  and  $k_2$  are equal and opposite the surface is a perfect saddle. This too comprises its own special class of surfaces, known as ‘minimal surfaces’, which have arisen in models for optimization of surface area in self-organizing systems such as soap foams, cell membranes, and crystal lattices (Osserman, 2013). The existence of approximate perfect saddles could be explored in a geomorphologic context by assigning a threshold below which curvature variation is assumed negligible.

180 Again, we do not endeavor to explore this here, instead focusing on the 4 basic shape classes that can be assigned based on raw curvature calculations. This will provide us with sufficient information to quantify patterns in landscape curvature, and relate these to the evolution of geomorphic process regimes with upstream drainage area.

### 3.3 Finding the principal curvatures

Defining curvature rigorously on discretely sampled topography requires accounting for changes in surface orientation between neighboring points, and how that change is scaled by non-uniform distances on a complicated surface. Our derivation of principal curvatures largely follows Struik (1950), though we will point to complementary references throughout. First, a position on the surface is taken to be the endpoint of a position vector parameterized by  $uv$ -coordinates such as those shown in Fig. 2.b, but referenced to a Cartesian basis via as

$$\mathbf{r}(u, v) = r_1 \hat{\mathbf{e}}_1 + r_2 \hat{\mathbf{e}}_2 + r_3 \hat{\mathbf{e}}_3 \quad (6)$$

190 where the  $\hat{\mathbf{e}}_i$  are unit vectors corresponding to easting, northing, and elevation, and  $u$  and  $v$  are coordinates following any two intersecting curves on the surface. In this case the  $uv$ -coordinates follow the lines on the map-view grid, but we do not assume

orthogonality on the surface. The square of the infinitesimal arc-length between points is then given by

$$I = ds^2 = d\mathbf{r} \cdot d\mathbf{r} = Edu^2 + 2Fdudv + Gdv^2 \quad (7)$$

where  $E = \frac{\partial \mathbf{r}}{\partial u} \cdot \frac{\partial \mathbf{r}}{\partial u}$ ,  $F = \frac{\partial \mathbf{r}}{\partial u} \cdot \frac{\partial \mathbf{r}}{\partial v}$ , and  $G = \frac{\partial \mathbf{r}}{\partial v} \cdot \frac{\partial \mathbf{r}}{\partial v}$  (the metric coefficients) quantify the proportionality of distances measured on the surface to distances in the Cartesian reference frame. They can also be used to calculate the ratio of area on the surface to pixel area as  $\alpha = \sqrt{EG - F^2}$ , a quantity we will use to calculate intrinsic drainage areas in our analysis (Sect. 4).

Equation 7, known as the first fundamental form or surface metric formula, allows us to accurately calculate distances and areas on the surface. This in turn can be used to scale topographic curvatures. Curvatures are calculated as a change in surface orientation along a path, defined as

$$II = d\mathbf{r} \cdot \mathbf{N} = edu^2 + 2fdudv + gdv^2, \quad (8)$$

where  $e = \frac{\partial^2 \mathbf{r}}{\partial u^2} \cdot \mathbf{N}$ ,  $f = \frac{\partial^2 \mathbf{r}}{\partial u \partial v} \cdot \mathbf{N}$  and  $g = \frac{\partial^2 \mathbf{r}}{\partial v^2} \cdot \mathbf{N}$  (the curvature coefficients) are the projection of directional curvatures onto a unit normal vector

$$\mathbf{N} = \frac{\frac{\partial \mathbf{r}}{\partial u} \times \frac{\partial \mathbf{r}}{\partial v}}{\left| \frac{\partial \mathbf{r}}{\partial u} \times \frac{\partial \mathbf{r}}{\partial v} \right|}. \quad (9)$$

Equation 8 is called the second fundamental form, and measures changes in the orientation of the tangent plane along  $ds$ . Combining the information in Eqs. 7 and 8 as

$$\kappa = -\frac{II}{I} = -\frac{d\mathbf{r}}{ds} \cdot \frac{d\mathbf{N}}{ds} = -\frac{edu^2 + 2fdudv + gdv^2}{Edu^2 + 2Fdudv + Gdv^2} \quad (10)$$

allows us to completely define the shape of a surface in 3-d space. Resultant curvature values reference the Cartesian coordinate system given by the map grid, but without the assumption of orthogonality on the surface that otherwise leads to projection distortion. The coefficients of the second fundamental form ( $e, f$  and  $g$ ; eq. 8) are the directional curvatures where  $e$  and  $g$  correspond to curvature along the E-W and N-S grid line respectively, and  $f$  is a cross term that accounts for directional covariance. These values are scaled by the coefficients of the first fundamental form ( $E, F$ , and  $G$ ; eq.7), which maps lengths on the coordinate grid to lengths on the surface accounting for the effect of slope on surface distances.

The directions of the principal curvatures can be found algebraically by defining a parameter  $\lambda = dv/du$  and rewriting Eq. 10 as

$$\kappa = \frac{edu^2 + 2f\lambda du^2 + g\lambda^2 du^2}{Edu^2 + 2F\lambda du^2 + G\lambda^2 du^2} = \frac{e + 2f\lambda + g\lambda^2}{E + 2F\lambda + G\lambda^2}. \quad (11)$$

Since the principal curvatures correspond to extrema where  $d\kappa/d\lambda = 0$  we differentiate eq. 11 with respect to  $\lambda$  and set the result equal to zero. The result is given by

$$\frac{d\kappa}{d\lambda} = (E + 2F\lambda + G\lambda^2)(f + g\lambda) - (e + 2f\lambda + g\lambda^2)(F + G\lambda) = 0. \quad (12)$$

220 Rearranging Equation 12 gives

$$(Fg - Gf)\lambda^2 + (Eg - Ge)\lambda + (Ef - Fe) = 0, \quad (13)$$

a quadratic equation in  $\lambda$  whose roots correspond to the principal curvature directions. Recalling that  $\lambda = dv/du$  we can equate these values to angles in our local  $uv$ -coordinate system and can thus reference principal curvature orientations within the map-view grid.

225 Magnitudes of the principal curvatures can be found through a similar approach. Since  $d\kappa/d\lambda = 0$  along the principal directions, 11 and 12 can be combined to give a simpler expression for the curvature

$$\kappa = \frac{f + g\lambda}{F + G\lambda}. \quad (14)$$

Recognizing that

$$E + 2F\lambda + G\lambda^2 = (E + F\lambda) + \lambda(F + G\lambda) \quad (15)$$

230 and

$$e + 2f\lambda + g\lambda^2 = (e + f\lambda) + \lambda(f + g\lambda), \quad (16)$$

eq. 12 can be rearranged to show

$$\kappa = \frac{f + g\lambda}{F + G\lambda} = \frac{e + f\lambda}{E + F\lambda}. \quad (17)$$

The two expression for curvature given by eq. 17 can be rearranged as

$$235 \quad f - \kappa F + \lambda(g - \kappa G) = 0 \quad (18)$$

and

$$e - \kappa E + f - \kappa F = 0, \quad (19)$$

respectively. Multiplying eqs. 18 and 19 by  $du$  (with  $\lambda = dv/du$ ) we arrive at a system of linear equations in our original  $uv$ -coordinate system

$$240 \quad \begin{bmatrix} e - \kappa E & f - \kappa F \\ f - \kappa F & g - \kappa G \end{bmatrix} \begin{bmatrix} du \\ dv \end{bmatrix} = \begin{bmatrix} 0 \\ 0 \end{bmatrix}. \quad (20)$$

This has a non-trivial solution only if the determinant of the coefficient matrix is zero. The corresponding quadratic equation in  $\kappa$

$$(EG - F^2)\kappa^2 - (gE - 2fF + eG)\kappa + (eg - f^2) = 0 \quad (21)$$

has roots that are the principal curvatures. By convention, we take the more positive of these roots to be  $k_1$ , while the less positive curvature is  $k_2$ . We also assume that positive curvatures are concave down.

245

### 3.4 Justification of the classical approach

It should be noted that here we have taken a deliberately classical approach to finding the principal curvatures and related invariants. Modern differential geometry is mostly based on tensor formulations, wherein the information contained in the first  
250 fundamental form is stored in the ‘metric tensor’

$$g_{ij} = \begin{bmatrix} E & F \\ F & G \end{bmatrix}, \quad (22)$$

and the information of the second fundamental form is stored in the ‘surface curvature tensor’

$$b_{ij} = \begin{bmatrix} e & f \\ f & g \end{bmatrix}. \quad (23)$$

Curvature invariants are extracted from the shape operator, a rank-2 tensor given by taking the negative gradient of a normal  
255 vector along an arbitrary tangent ( $S(\mathbf{t}) = -\nabla_{\mathbf{t}}\mathbf{N}$ ; O’Neill (2006)), or alternatively as the product of the inverse metric tensor and curvature tensor ( $S_j^i = g^{ik}b_{kj}$ ). The eigenvalues of the shape operator are the principle curvatures, and the eigenvectors define the directions associated with  $k_1$  and  $k_2$ . The Gaussian and mean curvatures are the determinant and half-trace of the shape operator, respectively.

An approach to DEM curvature analysis that utilizes the shape operator can be found in Mynatt et al. (2007) and Pearce et al.  
260 (2006), who apply a similar workflow to study structural geologic surfaces. While this approach has greater mathematical simplicity, we find it computationally expensive to do the required matrix operations at every DEM pixel, which limits the scale over which the method can be applied. For example, on a personal laptop, the calculation of curvatures on a  $1000 \times 1000$  cell DEM using a MATLAB code similar to that employed by Mynatt et al. (2007) took  $\sim 100$  times longer than the more classical approach outlined above. Given the size of topographic datasets, decreasing computation expense increases usability  
265 of the tool.

## 4 Computing curvatures on gridded DEMs

### 4.1 Spectral filtering of gridded datasets

In order to calculate DEM curvatures, it is necessary to do some degree of smoothing. This both removes artifacts of the grid-  
ding process, (Reuter et al., 2009; Bui and Glennie, 2023; Bater and Coops, 2009) and guarantees a continuous surface (Stewart,  
270 2003). We use 8.1 m resolution DEM data freely available through the National Map (<https://apps.nationalmap.gov/downloader/>). While higher resolution LiDAR (Light Detection and Ranging) data are available in the study area, the coarser dataset is sufficient for resolving geometric trends and ridge-valley landforms at the scale of fluvial basins.

There are many established approaches to DEM smoothing, including b-spline fitting (Brigham and Crider, 2022), wavelets (Struble et al., 2024), selective denoising (Gallant, 2011), and TIN interpolation (Jordan, 2007). We choose to filter the data

275 using a Discrete Fourier Transform (DFT; also a contribution of Gauss (Heideman et al., 1985)), which decomposes discretely  
sampled signals into sums of harmonic functions. Smoothing is accomplished via low-pass filtering, where information at  
wavelengths smaller than a defined cutoff is removed. Fourier methods have been extensively applied in geomorphology, with  
applications including the identification of characteristic process scales (Perron et al., 2008), landform identification (Booth  
et al., 2009), and assessing topographic controls on mass transport mechanics (Richardson and Karlstrom, 2019; Black et al.,  
280 2017; Crozier et al., 2018).

One challenge of Fourier methods is that harmonic functions do not naturally respect the finite nature of a DEM. Tapering of  
the data is thus required to obtain zero elevation at the boundaries prior to applying a DFT. It is common to accomplish this  
by convolving the DEM grid with a 2-d raised cosine (aka Hanning window), such that the resulting topography is equal to its  
actual value only in center of the grid, and is elsewhere damped towards the margins (Perron et al., 2008).

285 A downside of this approach is that it does not preserve the spectral power of landscape features. Luckily, this effect can be  
minimized by first reflecting the topographic grid along each coordinate axis, then tapering the data only in reflected portions  
that fall outside the limits of the original DEM McNutt (1983); Harris (1978). While spurious signals at wavelengths greater  
than the DEM are not eliminated, this windowing approach minimizes smaller scale distortion within the study area. We use a  
Tukey window (implemented as *window2* in Matlab), which consists of a boxcar function convolved with a cosine taper along  
290 the margins (Harris, 1978). Tapered regions thus fall outside the extent of the original DEM.

The Discrete Fourier Transform (DFT) is calculated as

$$Z(k_x, k_y) = \sum_{p=0}^{N_x-1} \sum_{q=0}^{N_y-1} z(p\Delta x, q\Delta y) e^{-2\pi i(\frac{k_x p}{N_x} + \frac{k_y q}{N_y})}, \quad (24)$$

where  $N_x$  and  $N_y$  are the number of grid cells in each direction,  $p$  and  $q$  are array indices,  $\Delta x$  and  $\Delta y$  are the grid spacings in  
each direction, and  $k_x$  and  $k_y$  are the wavenumbers in the respective x and y directions (Perron et al., 2008). Each value in the  
295 output array given by the above equation is associated with a frequency in  $x$  and  $y$  directions with magnitudes

$$f_x = \frac{k_x}{N_x \Delta x}, \quad f_y = \frac{k_y}{N_y \Delta y}. \quad (25)$$

These frequencies can then be used to define a radial frequency as

$$f_r = \sqrt{(f_x^2 + f_y^2)}. \quad (26)$$

The DFT periodogram is then given by

$$300 \quad P_f(k_x, k_y) = \frac{1}{N_x^2 N_y^2} |Z(k_x, k_y)|^2 \quad (27)$$

Following Perron et al. (2008) we apply a half-Gaussian filter based on radial frequencies

$$F_{low} = \begin{cases} 1, & f < f_1, \\ \exp\left(\frac{-(f-f_1)^2}{2\sigma^2}\right), & f \geq f_1, \end{cases} \quad (28)$$

where  $\sigma = \frac{1}{3}|f_2 - f_1|$  is the standard deviation. The filter is convolved with the radial frequency spectrum before the filtered spectrum is reverse transformed and the original domain of the DEM is extracted from the windowed representation to yield a  
 305 low-pass filtered raster of topography.

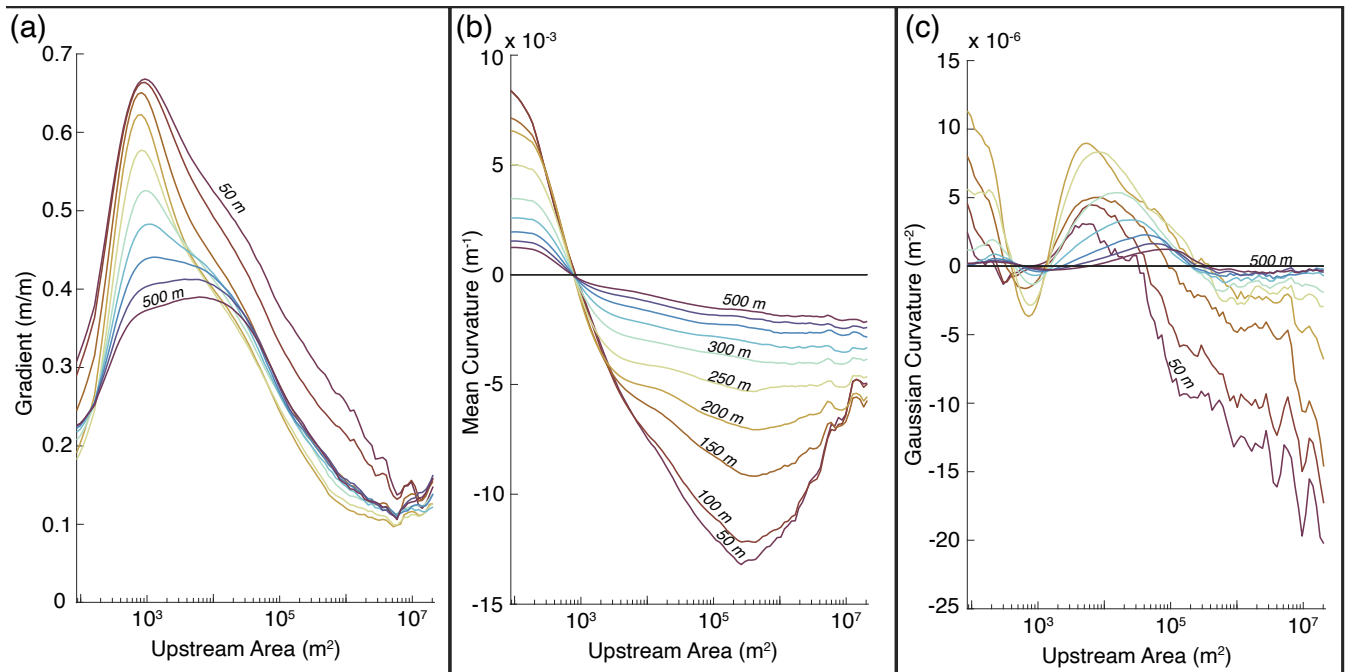
## 4.2 Selection of filtering scale

Once the landscape has been filtered, the invariant curvature metrics outlined in Sect. 3.2 and 3.3 are calculated on each DEM pixel. Curvature values are binned by drainage surface-area, calculated using the D-infinity algorithm (Tarboton, 1997) implemented in the TopoToolbox MATLAB function library (Schwanghart and Scherler, 2014), with pixel values weighted by  
 310 the surface area ratio ( $\alpha$ ) defined in Sect. 3.3. To explore the impact of low pass filter scale, we first smooth the landscape to 50 m, then increase the low-pass filter cutoff by increments of 50 m up to 500 m and look for shifting patterns in the area-space evolution of topographic geometry (fig. 4). While the magnitudes of curvature and slope vary with increased filtering, general trends in these metrics are similar across this range of filter cutoffs. This suggests that the filter cutoff parameter does not fundamentally alter landscape geometric structure. However, while the magnitudes of mean curvature decrease systematically  
 315 with increasing filter cutoff, the main extrema in Gaussian curvature have the greatest magnitudes at a cutoff of 200 m, perhaps indicating a characteristic curvature scale in the landscape. The slope distribution also suggest this as a scale of interest, as curves are pulled to lower drainage areas up to 200 m wavelengths at which point this trend reverses.

Based on these observations, we perform all further analysis on topography low-pass filtered to 200 m. This filter scale allows us to identify landscape features that span hillslope and fluvial process regimes, however inhibits our ability to see the effects  
 320 of finer scale processes (e.g., tree throw; Roering et al. (2010)). Map-view distributions of mean and Gaussian curvatures, principal curvatures, tangent plane slope, and upstream drainage area for a DEM filtered to 200 m are shown in Fig. 5.

## 5 A geometric view of Coast Range topography

As outlined in Sect. 3.2, mean and Gaussian curvature values can be used to classify each DEM pixel uniquely into four distinct shape classes: dome, basin, synformal saddle, and antiformal saddle (Fig. 3). We find that upstream drainage area provides a  
 325 natural way to study the resulting shape class distributions across the landscape, represented in Fig. 6.a by its probability density function (PDF). Figure 6.b shows PDFs of each shape class, which represents the probability of a shape class and given drainage area value occurring simultaneously ( $P(C \cap A)$ ). As the distribution of shapes is clearly weighted by the area distribution, we find it more informative to calculate the conditional probabilities of shapes classes (Fig. 6.c) by invoking the



**Figure 4. Surface geometry metrics binned by upstream drainage area for a range of low-pass filter cut-offs between 50 m and 500 m calculated on 50 m intervals. a. Gradient of tangent plane. b. Mean curvature ( $K_M$ ). c. Gaussian curvature ( $K_G$ ).**

probability axiom

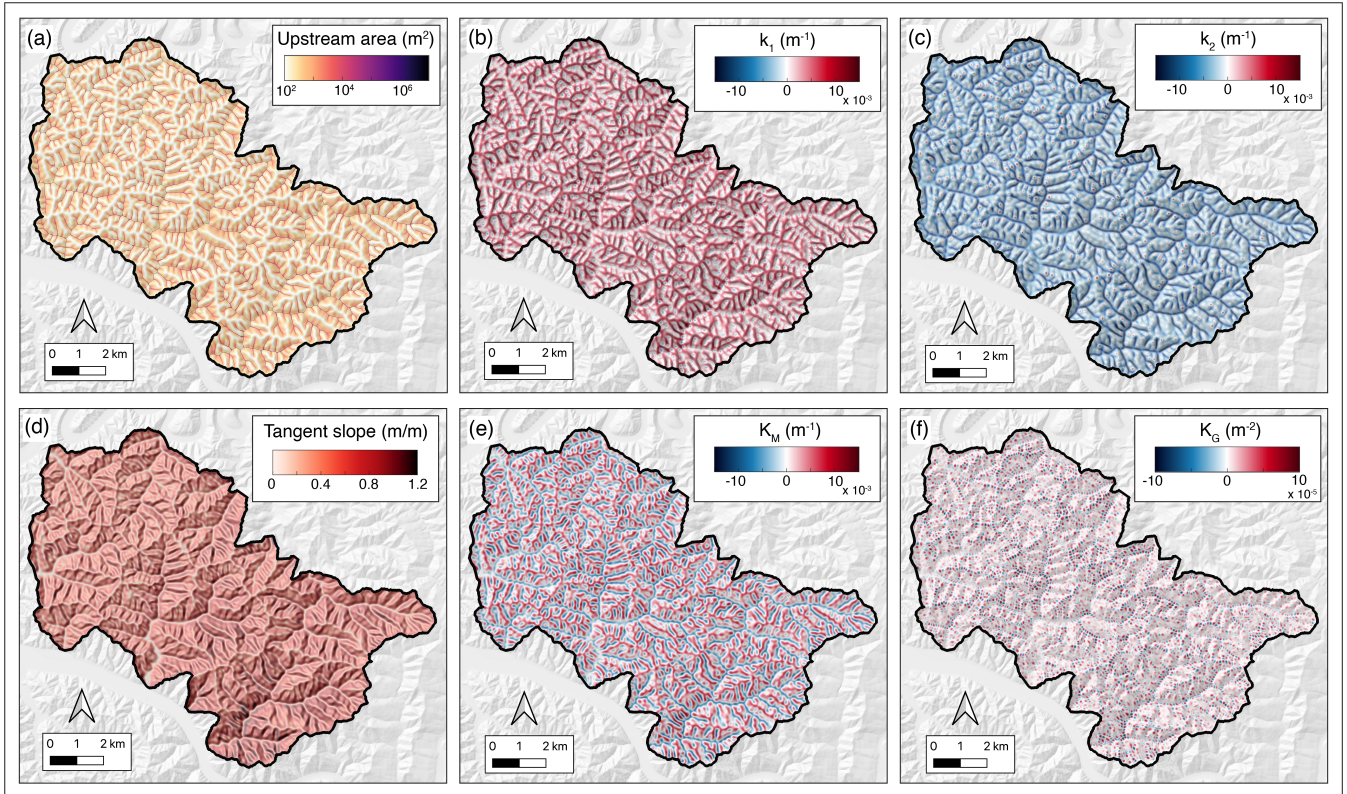
$$330 \quad P(C \cap A) = P(C|A)P(A) \rightarrow P(C|A) = \frac{P(C \cap A)}{P(A)}, \quad (29)$$

where  $P(C|A)$  is the conditional probability of shape class occurring given a value of  $A$ , and  $P(A)$  is the probability of pixel having a drainage area  $A$ .

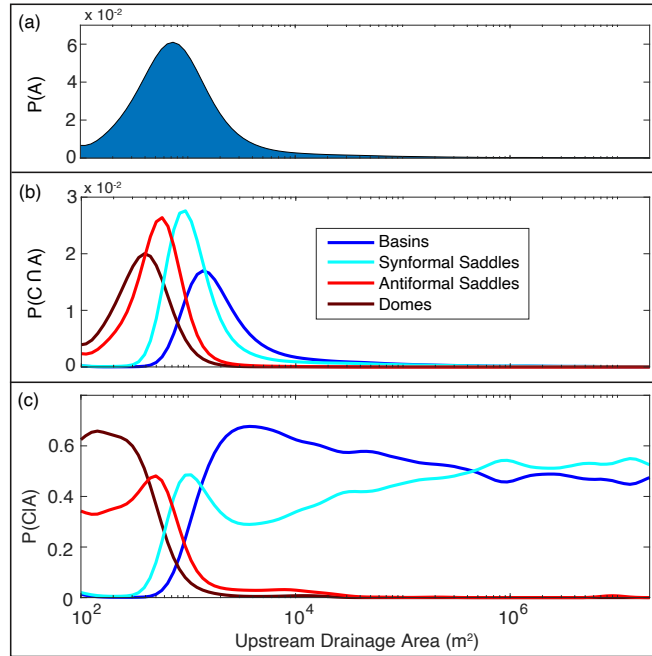
Figure 7 shows a compilation of basic geometric data extracted through our approach, represented in both area-space and map-view perspectives. While other potentially useful information can be extracted using this approach (such as the orientations and magnitudes of  $k_1$  and  $k_2$ ), we focus largely on curvature invariants to demonstrate the utility of curvature for identifying distinctive geometric properties of fluvial topography.

### 5.1 Landscape partitioning from Gaussian curvature

Noting significant and systematic variation in shape class distributions and curvature metrics with upstream drainage area (Fig. 340 7.a-c), we now explore landscape segmentation using inflection points in the mean and Gaussian curvatures. This is motivated by the physical assumption that signs of both  $K_M$  and  $K_G$  have implications for mass transport phenomena. The sign of  $K_M$  records the divergence versus convergence of local gradients, while the sign of  $K_G$  differentiates between stable and unstable



**Figure 5. Map-view distributions of surface geometry metrics.** **a.** drainage area of grid points calculated with D-infinity algorithm. Pixels are weighted with area-ratio  $\alpha$  to reflect drainage area on the topographic surface rather than the map-view projection. **b.** First principal curvature ( $k_1$ ). **c.** Second principal curvature ( $k_2$ ). **d.** Slope of tangent plane ( $S_T$ ). **e.** Mean curvature ( $K_M$ ). **f.** Gaussian curvature ( $K_G$ ).

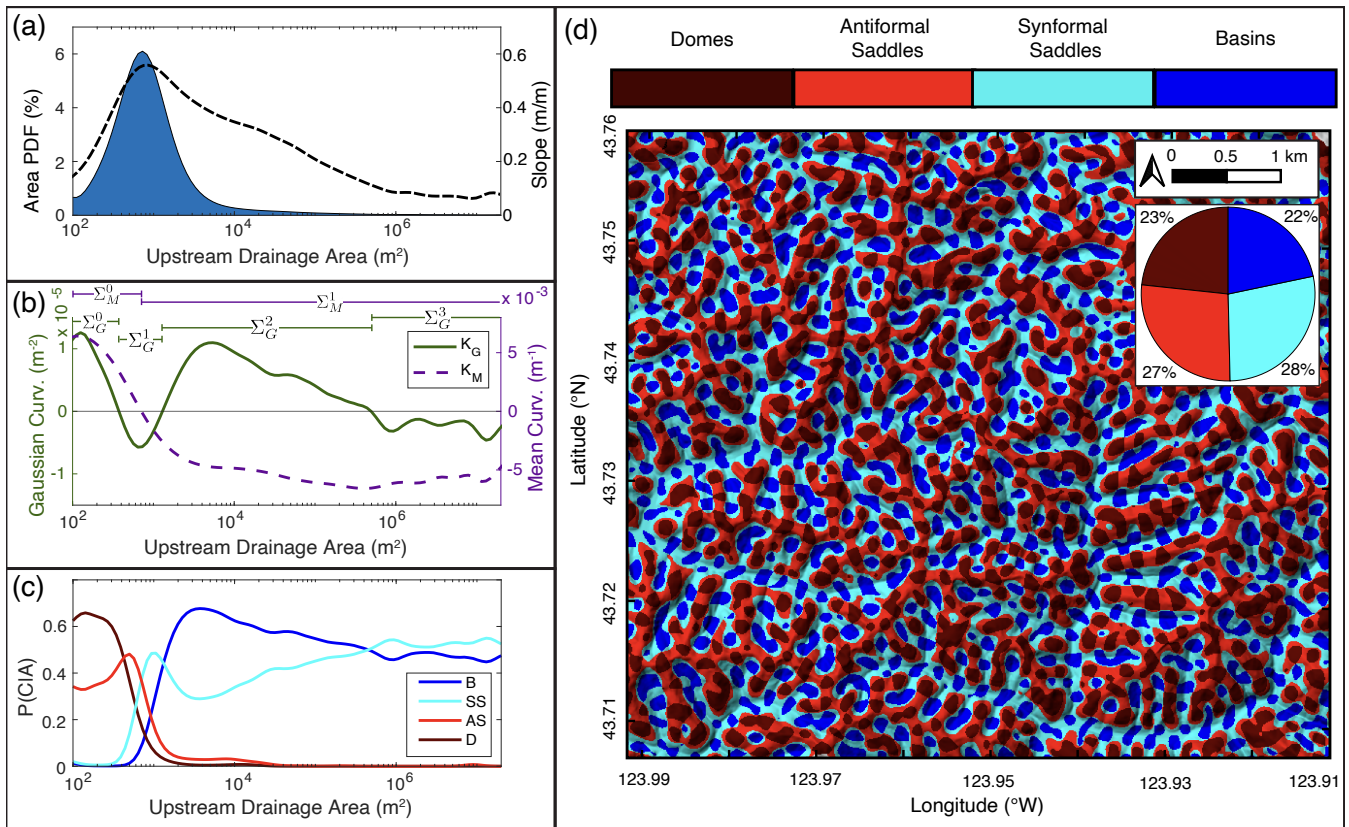


**Figure 6.** Shape class distributions as a function of drainage area. **a.** Probability density function of drainage areas within the region of interest. **b.** Probability density functions of shape classes as a function of drainage area. **c.** Conditional PDFs of shape classes at a given drainage area.

‘critical points’ that influence how the surface responds to disturbances (Goldsten et al., 2002; Matsumoto, 2001; Bonetti et al., 2018). As our partitioning approach is rooted in geometry we choose a labeling scheme  $\Sigma_i^j$  based solely on curvature invariants. Subscripts indicate the curvature used ( $i = G$  for  $K_G$  and  $i = M$  for  $K_M$ ), while superscripts ( $j$ ) correspond to the number of previous zero crossings in area space ( $j = 0$  corresponds to the zero crossing at smallest drainage area). This reference for curvature domains should facilitate future comparative studies of geometry across diverse tectonic, climatic, and lithologic settings.

### 5.1.1 $\Sigma_G^0$ : drainage areas less than $3.50 \times 10^2 \text{ m}^2$

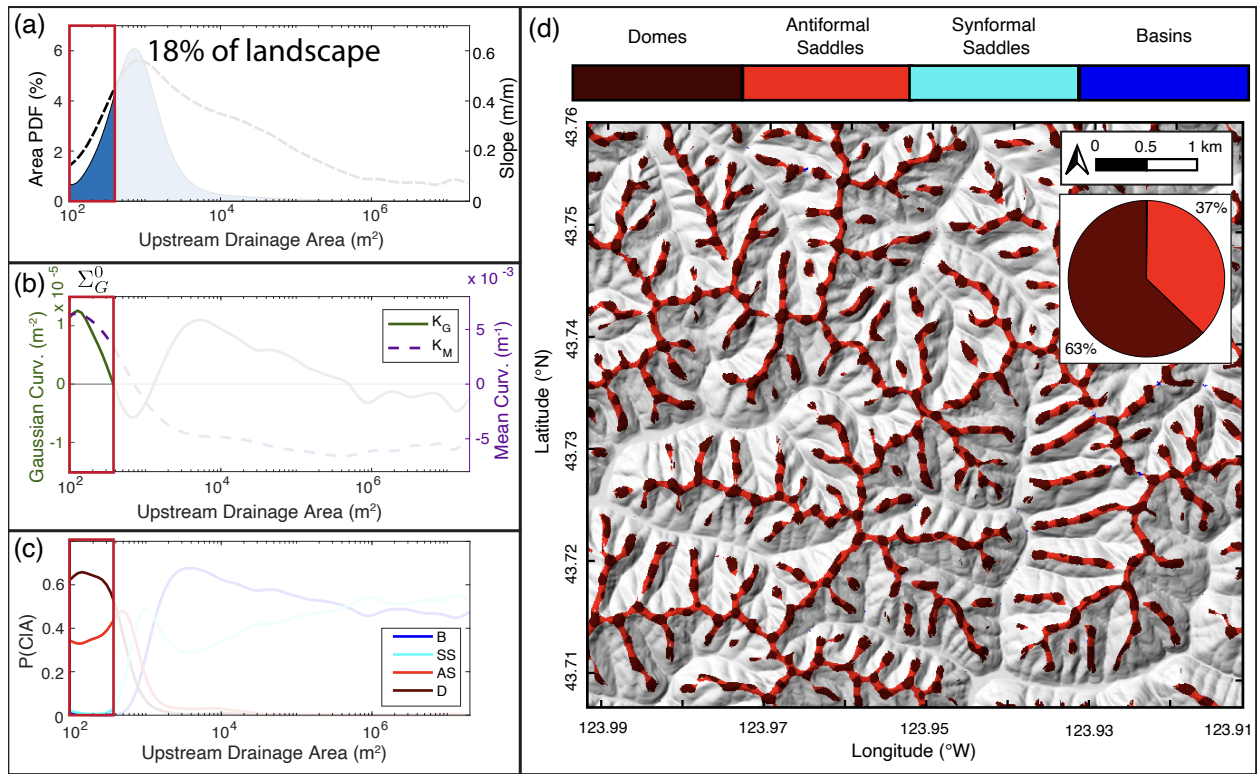
In fluvial landscapes, the smallest drainage areas are associated with the ridge-peak networks separating neighboring watersheds (Scherler and Schwanghart, 2019). We define a landscape region ( $\Sigma_G^0$ ) containing pixels with drainage areas less than  $3.75 \times 10^2 \text{ m}^2$ , the first area-space inflection in Gaussian curvature (Fig. 8.b). In this region, both curvature invariants are dominantly positive, reflecting downward concavity of topography and the divergence of surface gradient vectors (Dietrich et al., 1993; O’Neill, 2006). This is consistent with a region lacking convergent overland flow (Fenneman, 1908), where mass transport is accomplished through diffusive hillslope-transport processes. Large positive mean curvature here suggests high rates of diffusion required for erosion along ridge lines to keep pace with mass transport in channel networks below (Roering



**Figure 7.** Distribution of derived surface geometry metrics computed on the full region of interest. **a)** PDF of upstream drainage areas. Black dashed curve is slope binned by drainage area. **b)** Gaussian and mean curvatures binned by drainage area. Horizontal lines at top of panel show  $\Sigma$  regions outlined in Sect.s 5.1 and 5.2. **c)** Conditional PDFs of shape classes as a function of drainage area. **d)** Map of shape classes projected on a focused subregion of the study area. Pie-chart inset shows shape-class composition of the surface.

et al., 1999). This is supported by correlations between Laplacian curvature of hilltop regions and drainage-scale erosion rates elsewhere in the Oregon Coast Range (Struble et al., 2024).

360 Defined this way, the ridge-peak network makes up 18% of the land-surface (to 2 significant figures). Within this subregion, 63% of points are domal (peaks), with antiformal saddles (ridges) comprising the remaining 37% (Fig. 8.a,d). Along ridge lines this is expressed in oscillations between positive and negative Gaussian curvatures, analogous to the alternating “summits” and “knots” of Cayley (1859), and the “hills” and “passes” of Maxwell (1870). We will elaborate on this connection to early landscape organization theories in Sect. 5.3.

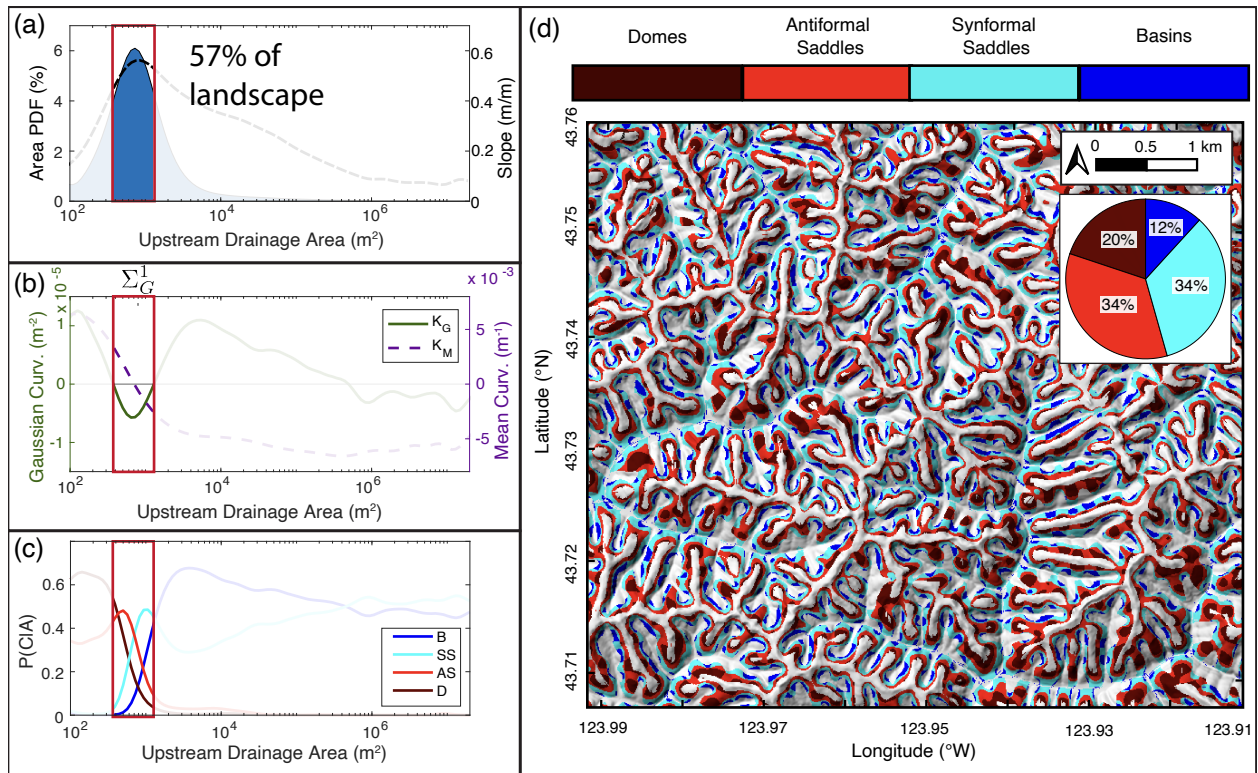


**Figure 8. Surface geometry data for region  $\Sigma_G^0$ : points in the landscape with upstream drainage areas less than  $3.50 \times 10^2 \text{ m}^2$ .** The red box in each of the area-binned plots (a-c) highlights the range of included drainage areas. **a)** PDF of drainage areas. **b)** Gaussian and mean curvatures binned by area. **c)** Conditional PDFs of shape classes. **d)** Map of shape classes projected on a focused subregion of the study area. Pie-chart inset shows shape-class composition of the surface.

### 365 5.1.2 $\Sigma_G^1$ : Drainage areas between $3.50 \times 10^2 \text{ m}^2$ and $1.29 \times 10^3 \text{ m}^2$

As drainage area increases above  $350 \text{ m}^2$ , the binned Gaussian curvature changes sign and is negative up to areas of  $1290 \text{ m}^2$  (Fig. 9.b). Fifty-seven percent of the land surface falls within this relatively narrow range of drainage areas, making it the largest of the  $\Sigma_G^j$ . This region is defined by high topographic gradients (Fig. 9.a), coinciding with hillslopes where loose material moves downhill through a combination of gradient-driven landsliding, granular creep, and stochastic raveling (Roering et al., 2001b; Jaeger and Nagel, 1992; Furbish et al., 2009; Deshpande et al., 2021; Gabet, 2003). Within this region, the point of minimum  $K_G$  coincides with the highest slopes in the landscape. It is associated with the only inflection point in mean curvature, marking the dominant concavity transition in the landscape. Such a concavity transition is required to connect almost uniformly divergent topography on hilltops ( $\Sigma_G^0$ ; Sect. 5.1.1) to convergent basins at the head of the drainage network ( $\Sigma_G^2$ ; Sect. 5.1.3). Geometrically, this manifests as rapid shape-class changes over a small range of drainage area (Fig. 9.c) and a more even split between the four shape classes overall (each shape class occupies  $\sim 10 - 30\%$  of the region), which suggests

375

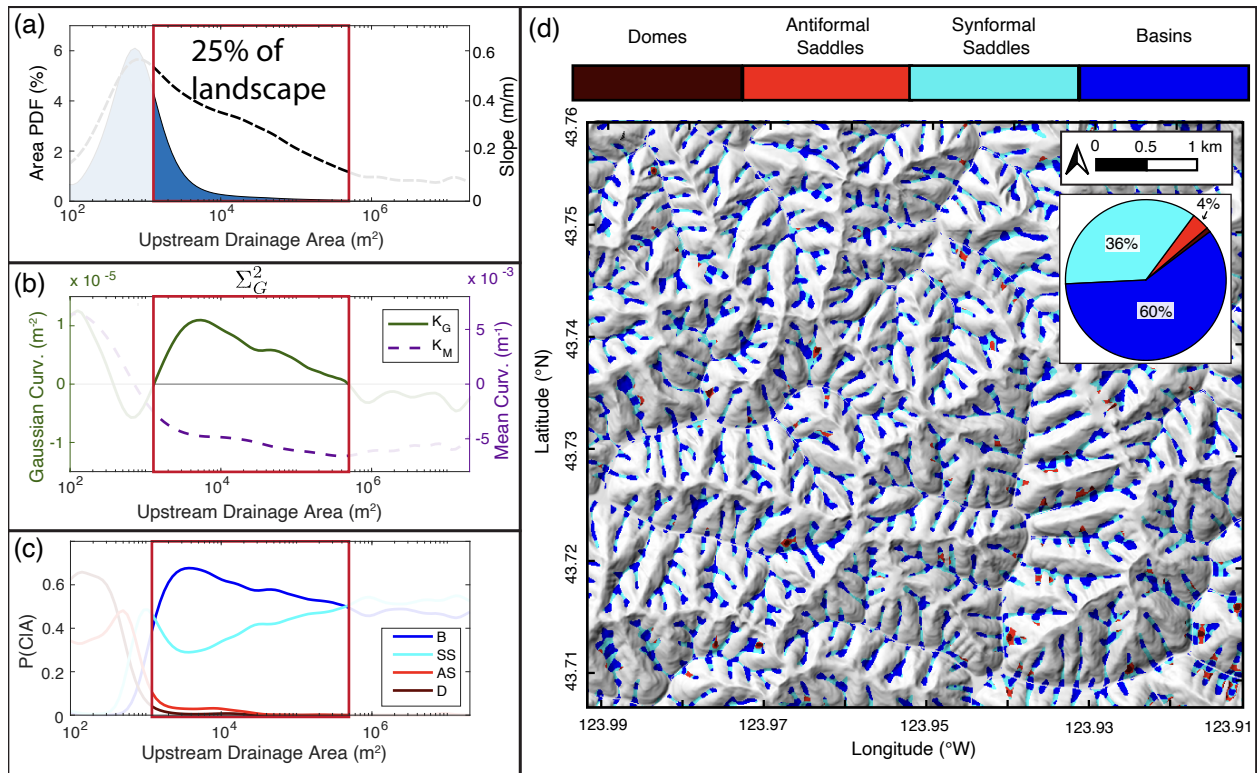


**Figure 9. Surface geometry data for region  $\Sigma_G^1$ :** points in the landscape with upstream drainage areas between  $3.50 \times 10^2 \text{ m}^2$  and  $1.29 \times 10^3 \text{ m}^2$ . The red box in each of the area-binned plots (a-c) highlights the range of included drainage areas. **a)** PDF of drainage areas. **b)** Gaussian and mean curvatures binned by area. **c)** Conditional PDFs of shape classes. **d)** Map of shape classes projected on a focused subregion of the study area. Pie-chart inset shows shape-class composition of the surface.

a high level of surface complexity across this concavity transition, consistent with previous inference based on topographic contour curvature (Bonetti et al., 2018).

### 5.1.3 $\Sigma_G^2$ : drainage areas between $1.29 \times 10^3 \text{ m}^2$ and $3.80 \times 10^5 \text{ m}^2$

At drainage areas of  $1.29 \times 10^3 \text{ m}^2$ , the Gaussian curvature again changes sign, increasing to a local maximum at  $\sim 4500$    
 380  $\text{m}^2$  before steadily returning to zero at  $3.30 \times 10^5 \text{ m}^2$  (Fig. 10.b). We define our third landscape region ( $\Sigma_G^3$ ) between these inflection points. Here, convergence of surface gradient vectors is indicated by negative  $K_M$  and the dominance of basins (60%) and synformal saddles (36%). This geometry intuitively implies colluvial hollows, where unconsolidated material collects at the head of debris-flow networks (Dietrich et al., 1993). At drainage areas exceeding that of the local maximum in Gaussian curvature, the decrease in both  $K_G$  and  $K_M$  is consistent with increasing downstream channelization in debris-flow channels   
 385 (Stock and Dietrich, 2003; Mcguire et al., 2022). This same trend is apparent in the shape class distributions in Fig. 10.c, where basins trade off with synformal saddles surface gradient vectors converge. This region makes up 25% of the study

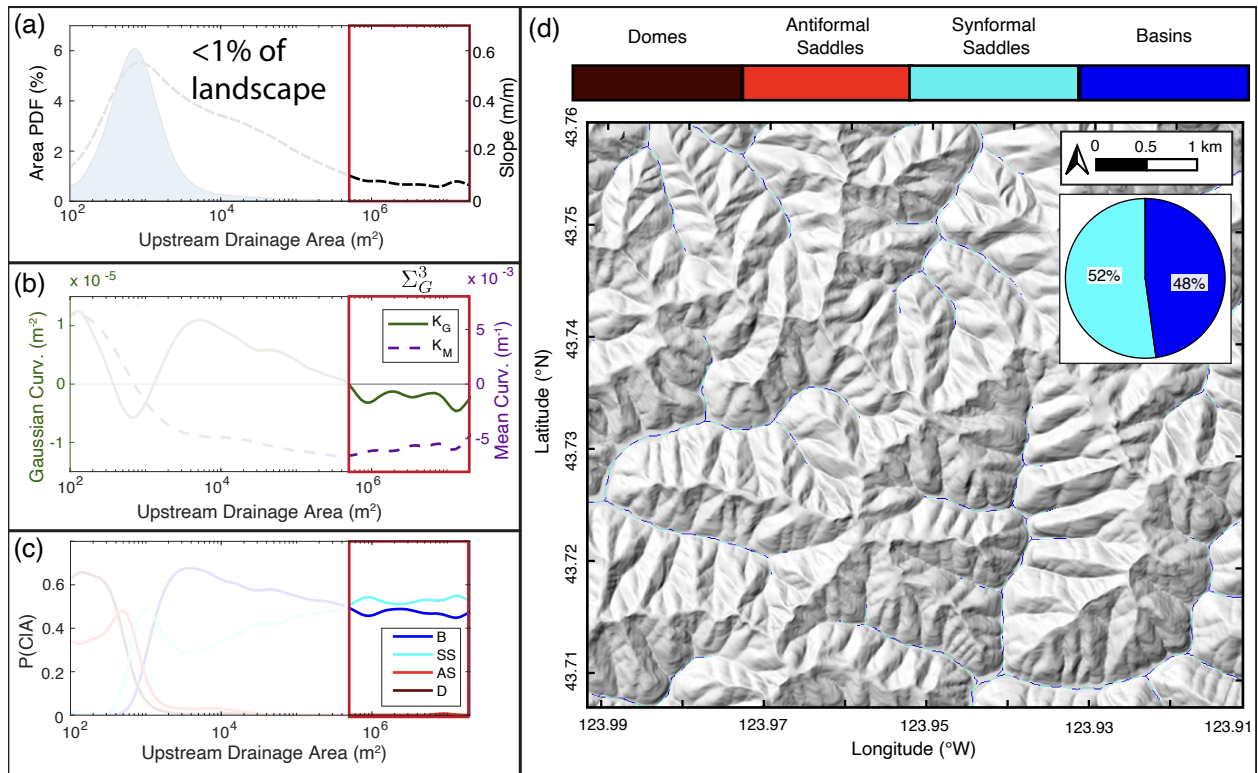


**Figure 10.** Surface geometry data for region  $\Sigma_G^2$ : points in the landscape with upstream drainage areas between  $1.29 \times 10^3 \text{ m}^2$  and  $3.80 \times 10^5 \text{ m}^2$ . The red box in each of the area plots highlights the region of interest. **a)** PDF of drainage areas. **b)** Gaussian and mean curvatures binned by area. **c)** Conditional PDFs of shape classes. **d)** Map of shape classes projected on a focused subregion of the study area. Pie-chart inset shows shape-class composition of the surface.

area, slightly more than the 18% of the landscape encapsulated by the other region of positive Gaussian curvature ( $\Sigma_G^0$ , the ridgeline network). In addition, the percent composition of basins (60%) and synformal saddles (36%) roughly mirrors the  $\Sigma_G^0$  composition of domes (63%) and antiformal saddles (37%) in  $\Sigma_G^0$ , a symmetry that will be discussed further in Sect. 5.2.

#### 390 5.1.4 $\Sigma_G^3$ : drainage areas greater than $3.80 \times 10^5 \text{ m}^2$

The last inflection point in Gaussian curvature occurs at drainage areas of  $3.80 \times 10^5 \text{ m}^2$ , where synformal saddles surpass basins as the dominant morphology (Fig. 11.c). The growing influence of channels in defining landscape curvature suggests the dominance of fluvial erosion, an interpretation that is consistent with area-space fluvial transitions inferred elsewhere in the literature (Montgomery and Foufoula-Georgiou, 1993). The spatial contribution of this region is extremely small ( $< 1\%$  of the land surface; Fig. 11.a), with little geometric change across the two orders of magnitude spanned by drainage area. The only overall trend is a gradual increase in mean curvature, which could indicate downstream valley widening as erosional efficiency increases. However, a close look at the map-view shape distribution (Fig. 11.d) reveals regular transitions between basin and



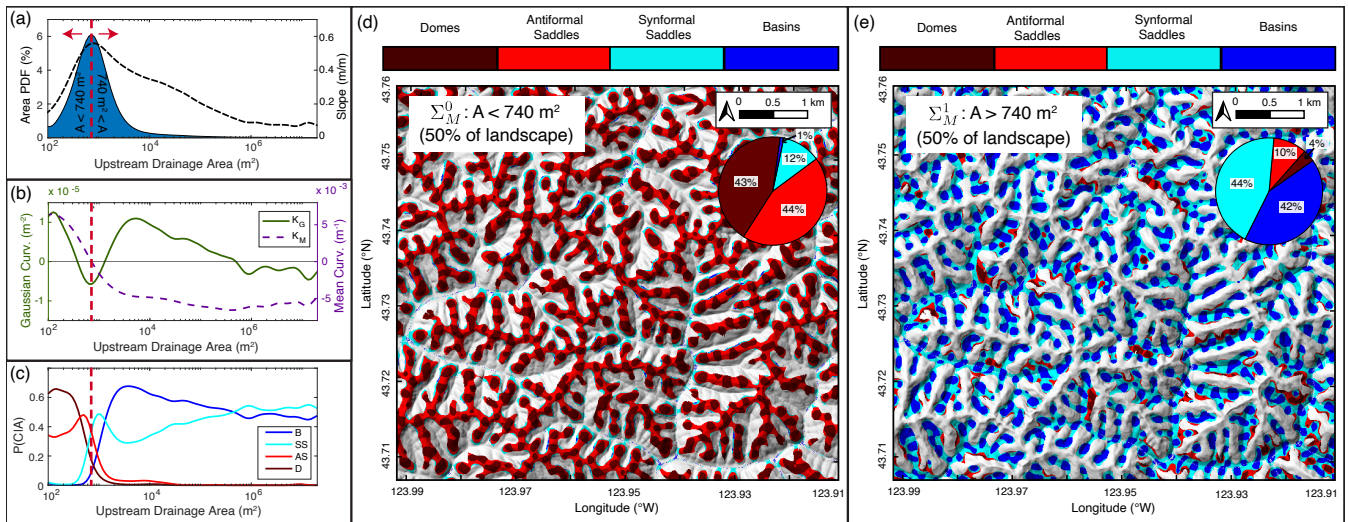
**Figure 11. Surface geometry data for region  $\Sigma_G^3$ : points in the landscape with upstream drainage areas greater than  $3.80 \times 10^3 \text{ m}^2$ .** The red box in each of the area plots highlights the region of interest. **a)** PDF of drainage areas. **b)** Gaussian and mean curvatures binned by area. **c)** Conditional PDFs of shape classes. **d)** Map of shape classes projected on a focused subregion of the study area. Pie-chart inset shows shape-class composition of the surface.

saddle structures, indicating along-channel oscillations in the first principal curvature ( $k_2$  is always negative in a channel) – another observation connecting our analysis to the ideas of Cayley and Maxwell that we will revisit and discuss in Sect. 5.3.

400 While all of the process regimes identified in this Gaussian curvature decomposition have been previously identified in the literature (e.g. Montgomery and Buffington (1997)), it is remarkable how clearly this single intrinsic metric captures the full range of process transitions in a fluvial landscape.

## 5.2 Landscape partitioning from mean curvature

In this section we show that mean curvature also provides a way of understanding connections between geometry and process  
 405 in fluvial topography. We decompose the landscape into two regions ( $\Sigma_M^0$  and  $\Sigma_M^1$ ) separated by the single inflection in  $K_M$  at drainage areas of  $740 \text{ m}^2$ . Results are shown in Fig. 12. Alignment between this point in area-space and the peak of the slope curve in Fig. 12.a is consistent with the idea that curvature decreases as hillslope profiles approach an angle-of-repose ( $\sim 30^\circ$



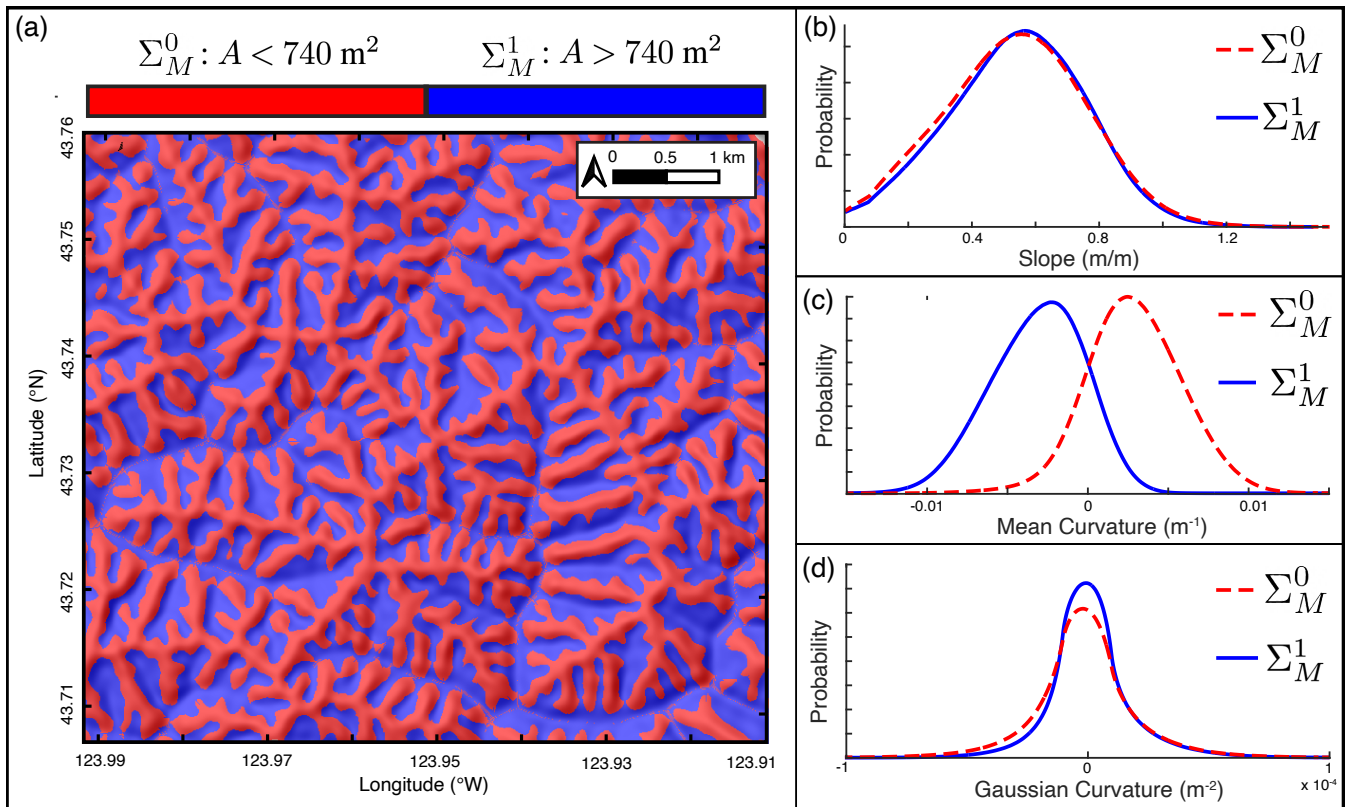
**Figure 12. Maps of surface geometry for landscape partitioning about the mean curvature inflection point at drainage areas of 740 m<sup>2</sup>. Red-dashed lined shows location of curvature inflection point. a) PDF of drainage areas. b) Gaussian and mean curvatures binned by area. c) Conditional PDFs of shape classes. d) Map of shape classes for drainage areas less than 740 m<sup>s</sup>. e) Map of shape classes for drainage areas greater than 740 m<sup>s</sup>. Pie-chart insets on panels d and e show shape-class compositions of the surfaces.**

inferred from the peak of the slope curve in Figs. 7-11), above which loose material is gravitationally unstable (Roering et al., 2007). Downhill of this point, slope decreases and unconsolidated material will tend to collect as colluvium at the head of the channel network (region  $\Sigma_C^2$ ).

Partitioning the landscape this way reveals surprising symmetries in both shape class distributions and surface geometry metrics for the two regions (Fig. 12.d-e). The landscape is equally distributed about this zero crossing. For our filtering method and scale, 50% of points are above or below the most probable drainage area value in our study area. Figure 13.a shows a map of the study area divided into concave and convex domains based on this area threshold. Probability distributions of slope, mean curvature, and Gaussian curvature for the two regions are shown in Fig. 13.b-d. While the slope and Gaussian curvature are similarly distributed in the concave and convex landscape regions, we see that the mean curvature has mirrored distributions such that the integrated mean curvature in the landscape is approximately zero.

### 5.3 Geometric properties of channels and ridges

We have thus far focused on documenting Oregon Coast Range landscape segmentation in drainage area from a curvature perspective. A clear corollary to this is to ask specifically about the emergent channel and ridge network structures that manifest from this drainage area segmentation. It is well established that curvature provides a powerful tool for extracting continuous concave-up structures and deriving definitions of channel networks that are self-consistent throughout the landscape (Passalacqua et al., 2010; Gallant and Hutchinson, 2011; Bonetti et al., 2018). Our methods are suitable for this task as well, and for the



**Figure 13. Distribution of surface geometry metrics for regions defined by the mean curvature inflection point.** **a.** Map-view of landscape partitioned about the point of inflection in  $K_M$ . **b.** Distribution of tangent slope in regions of both negative and positive average  $K_M$ . **c.** Distribution of mean curvature in regions of both negative and positive average  $K_M$ . **d.** Distribution of Gaussian curvatures in regions of both negative and positive average  $K_M$

parallel extraction of concave-down ridge network structures (Scherler and Schwanghart, 2019), but we will not pursue that  
 425 objective here.

Instead, we will focus on the strikingly even partitioning of mean curvature between concave up structures (channels) and  
 concave down structures (ridges). These structures are themselves composed entirely of alternating basins and synformal  
 saddles (in channels) and domes and antiformal saddles (on ridges). Figure 14.a shows a close-up of our study area around  
 Franklin Creek to demonstrate this pattern. While the size distribution of these alternating shape classes within a channel or  
 430 ridge is variably sensitive to lowpass filter threshold, the shape classes themselves are much more robust as they reflect zero  
 crossings in  $K_M$  and  $K_G$  whose positions are insensitive to filter cutoff (Fig. 4), particularly in the case of mean curvature. This  
 alternating pattern of local shape classes, originally recognized qualitatively by Cayley (1859) and Maxwell (1870), manifests  
 clearly in channel and ridge network geometry.

Fig. 14.b-c plots in blue the elevation of Franklin Creek and its south ridge as a function of distance from the most downstream point of the creek (where it intersects the Umpqua river). The drainage area (red curves) along these structures (calculated using the intrinsic area calculation method in Sect. 6.3) reflects expectations: discontinuities in drainage area along the channel correspond to tributary junctions while ridge-top drainage area deviates from one grid cell only in saddles (up to 8 grid cells long here) between local maxima.

Fig. 14.d-e plots the signed principle curvatures for ridge and channel. An immediate comparison of note is that local minima in  $k_1$  for the channel and  $k_2$  for the ridge correspond to basins and antiformal saddles respectively (circles). These structures align with tributary junctions in the channel, and lie directly upslope of 1st order channel heads on the ridge. This indicates that the curvature shape classes reflect structural changes in network geometry for both concave and convex topography. Neither structure – the local basins at channel junctions or saddles on ridgetops corresponding to transitions from hillslopes to channels – have been previously described to our knowledge. As these geometries describe changes in curvatures associated with branching structures in channels and ridges their locations are minimally sensitive to filter cutoff.

Fig. 14.f-g then plots the Gaussian ( $K_G$ ) and mean ( $K_M$ ) curvatures along the channel and ridge. The notable comparison in this case is that local maxima in  $K_G$  and  $K_M$  are anticorrelated along the channel and correlated along the ridge. This symmetry reflects the paired shape classes in either structure.

Comparing channel and ridge geometries we see that, in both cases, the two measures of curvature (principle curvatures or invariants) are near mirror-images of each other. One metric oscillates around zero (a principle curvature in 14.d-e and  $K_G$  in 14.f-g), while the other is strictly positive (for ridge) or negative (for channel), although still oscillatory. The along-channel and along-ridge envelope of this latter metric varies non-monotonically as expected for a small dendritic drainage basin, but also exhibits coincident channel widening (decrease in the magnitude of  $k_2$ ) and ridge narrowing (increase in  $k_1$  towards the mouth of Franklin Creek (distances  $\lesssim 2300$  m).

Finally, while process-based modeling of curvature is outside the scope of this work, it is informative to compare the observed curvature of channel and ridge to theoretical models. Fig. 14.c-E show best fitting power laws to ridge and channel, after (Whipple and Tucker, 1999) for bedrock channel longitudinal profile and models such as those of Willett (2010) for interfluvial ridge elevations. The fit constants are  $a = 6$  m,  $b_1 = 2.84 \times 10^{-7} \text{ m}^{-1.4}$ ,  $c_1 = -1.4$ ,  $b_2 = 41.88 \text{ m}^{0.72}$ ,  $c_2 = 0.28$ .

For Franklin Creek, while the elevation profile is well-approximated by a stream power-law fit, the resulting curvature (obtained by differentiating the longitudinal profile twice with respect to alongstream distance  $x$ ) does not capture oscillations observed in  $k_1$ , the along-channel principal curvature. And yet the average value of the stream power model curvature ( $1.1 \times 10^{-5} \text{ m}^{-1}$ ) is close to the average value of  $k_1$  ( $8.3 \times 10^{-5} \text{ m}^{-1}$ ) extracted from the DEM (we expect an even closer match if tributaries are included in the stream power model, e.g., Willett (2010)). Thus, the steady state model approximates the average concavity of the true channel geometry, despite much larger curvature oscillations associated with local basin structures at tributary junctions.

Similarly, a power-law fit to the Franklin Creek south ridge profile in Fig. 14.c well represents the elevation but fails to capture the smaller scale curvature oscillations between domes and antiformal saddles. The average value of this fit ( $-3.3 \times 10^{-4} \text{ m}^{-1}$ ) is within 7% of the average value of  $k_2$  ( $-3.5 \times 10^{-4} \text{ m}^{-1}$ ) extracted from the DEM, reflecting the overall concave down nature of the along-ridge curvature. These results suggest that standard fluvial process models, while missing  
470 physical ingredients at smaller scale, capture network-scale curvatures of channels and ridges.

## 6 Comparison to common metrics of topographic geometry

In this work, we have proposed a self-consistent means of defining several geometrical aspects of topography through connection to formal surface theory. We will now draw quantitative comparisons to some other commonly used metrics. We do this in an effort to highlight potential advantages of the invariant approach acknowledging, of course, that simpler methods  
475 are sometimes appropriate. Our goal is not to supplant other approaches, but rather to point out opportunities for increased adoption of an intrinsic reference frame in topographic analysis.

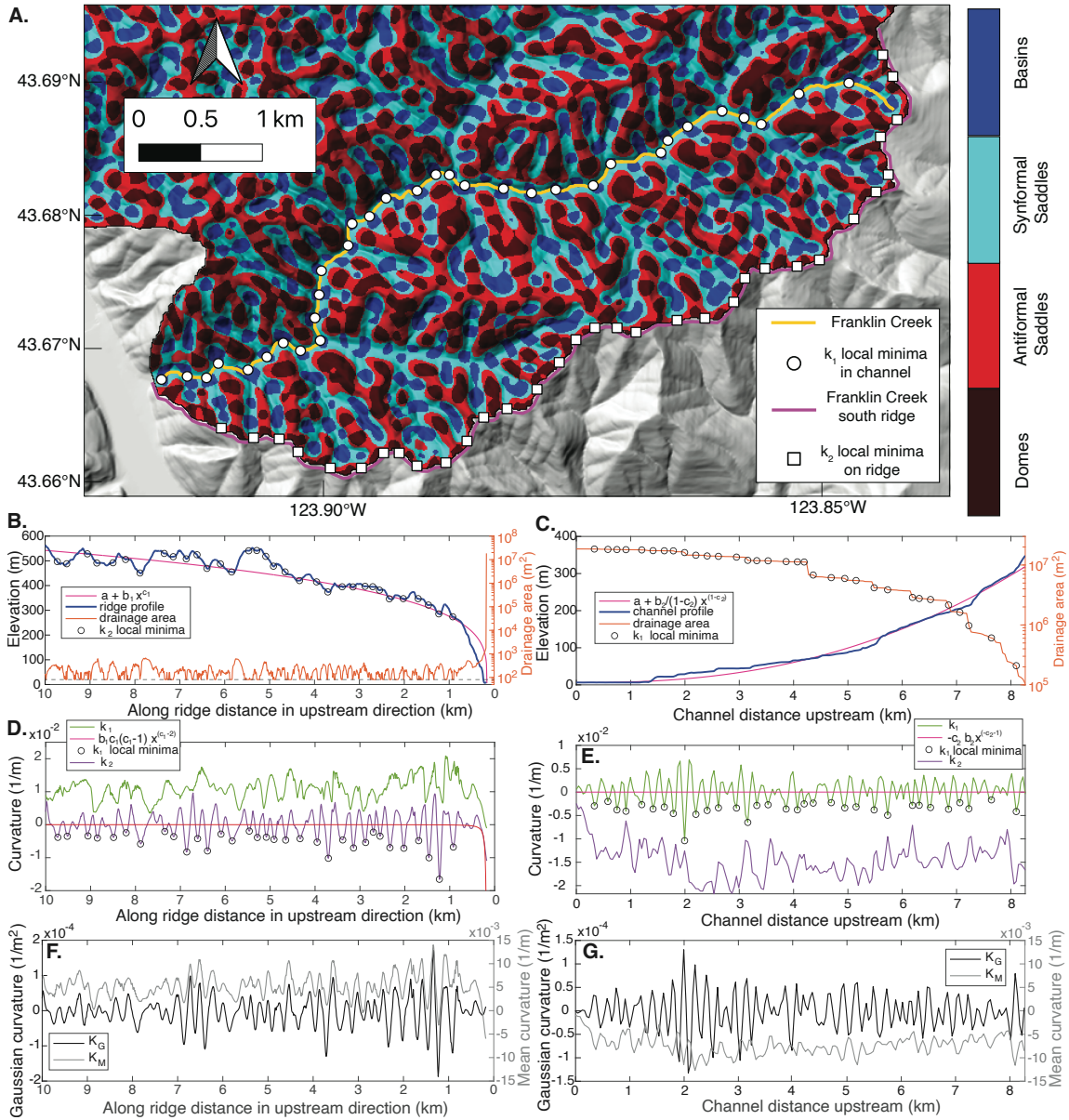
### 6.1 Comparison of mean and Laplacian curvatures

As outlined in Sect. 1.1, ‘curvature’ in geomorphology is often taken as synonymous with the output of the Laplacian operator, which arises from mass-continuity equations on hillslopes (Fernandes and Dietrich, 1997). We can understand the relationship  
480 between the Laplacian and  $K_M$  through consideration of Euler’s Theorem (Eq. 3), which shows that  $K_M$  is the average of curvatures measured along any two orthogonal paths on the surface. In cases where the  $x$  and  $y$  coordinate vectors are perpendicular on the surface, the relationship between the Laplacian and mean curvatures is (compare to equation 4 which uses principal curvatures)

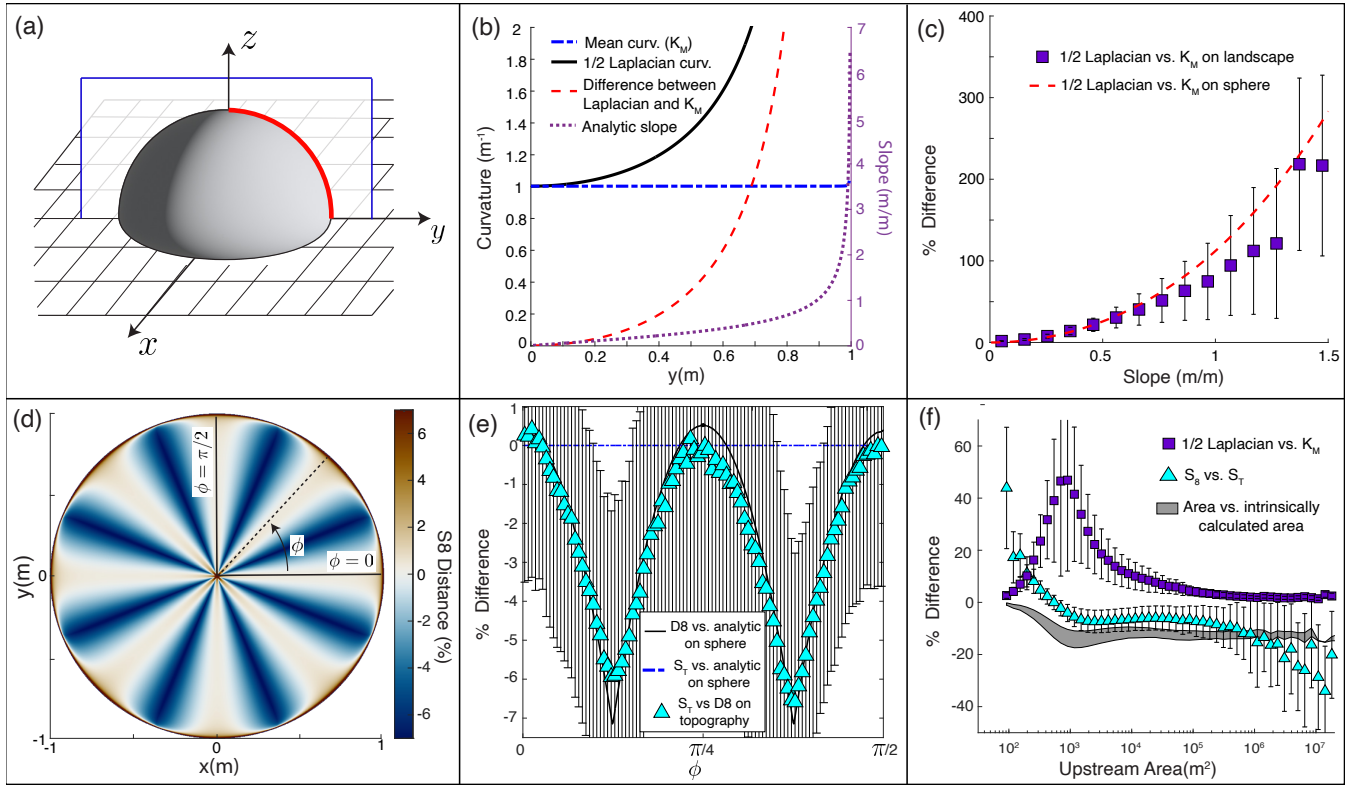
$$K_M = \frac{1}{2} \nabla^2 z. \quad (30)$$

485 However, deviations in orthogonality between coordinates on a map grid, and warping of distances in regions of high slope (Fig. 2), manifest in well-known projection errors (Minár et al., 2020; Bergbauer and Pollard, 2003). Figure 15.b and c compare the half-Laplacian calculated on a coordinate grid to the invariant mean curvature on a unit hemisphere and binned topographic data respectively. The observed slope-dependent deviation of the half-Laplacian from true curvature is dramatic in end-member cases but not of concern in many studies. It can be strategically avoided by focusing on low-slope regions (Struble et al., 2024),  
490 or evaluating curvature along 1-D hillslope profiles in which it is easier to account for slope effects (Roering et al., 2007). In addition, non-linear hillslope transport models only predict a direct correlation between curvature and erosion rates where slope is less than 30% or so, justifying the use of map-view Laplacian in regions where projection distortion is negligible (Hurst et al., 2012; Struble et al., 2024).

495 A formal approach has potential to strengthen such studies, however. In reality, there are few points in the landscape with zero slope. For example, the hilltop region identified in this study makes up 18% of the landscape (Sect. 8; Fig. 8). Roughly



**Figure 14. Characteristics of Franklin Creek and its south ridge.** (a) Curvature shape classes with channel and ridge highlighted in yellow and magenta. Circles are local minima of along-channel principal curvature  $k_1$  while squares are local minima of along-ridge principal curvature  $k_2$ . (b) Ridge elevation profile (left axis) and drainage area (right axis). Dashed line is drainage area for one cell. Pink curve is a powerlaw fit (fit parameters are listed in text). (c) Channel elevation profile (left axis) and drainage area (right axis). Pink curve is a powerlaw fit. (d) Principal curvatures along the south ridge. Note that local minima in  $k_2$  (black circles) correspond to local saddles directly upslope from 1st order channel heads in (a). The mean of  $k_1 = 0.01 \text{ m}^{-1}$  and the mean of  $k_2 = -3.49 \times 10^{-4} \text{ m}^{-1}$ . (e) Principal curvatures along Franklin Creek. Note that local minima in  $k_1$  (black circles) correspond to junctions between tributary channels in (a). The mean of  $k_1 = 8.32 \times 10^{-5} \text{ m}^{-1}$  and the mean of  $k_2 = -0.01 \text{ m}^{-1}$ . The red curve comes from stream power (it has a mean value of  $1.10 \times 10^{-5} \text{ m}^{-1}$ ). (f) and (g) Profiles of Gaussian curvature  $K_G$  and Mean curvature  $K_M$  along ridge and channel.



**Figure 15. Comparison of intrinsic surface metrics use in this study with other methods common in the literature. a.** Cartoon depiction of unit hemisphere used for comparison with topographic data. Red line shows curve along which error is evaluated in panel b. **b.** Comparison of Mean curvature ( $K_M$ ) and 1/2 Laplacian as a function of distance from the origin for plane curve defined by the intersection of the unit hemisphere with the  $y - z$  plane. Black line is 1/2 Laplacian, blue dashed line is Mean curvature calculated using intrinsic method, red dashed line is difference between 1/2 Laplacian curvature and the curvature of the sphere ( $1 m^{-1}$ ), and the purple dashed line is slope of the sphere. **c.** % error of the 1/2 Laplacian on the unit hemisphere and % difference between the 1/2 Laplacian and Mean curvature on topography binned as a function of slope. Red dashed line is % error on sphere and purple boxes are median values computed on topography. **d.** % error of the 8 point connected gradient computed on the unit hemisphere. **e.** % error of the 8 point connected gradient computed on the unit hemisphere and median % difference between  $S_8$  and  $S_T$  as a function of azimuth. **f.** % difference between our intrinsically calculated topographic metrics and other common methods as a function of drainage area.

half of this subset is at slopes above 0.4, where slope distortion in the Laplacian is around 20% (Fig. 15b-c). Selecting lower slope thresholds increases accuracy, but at the cost of data volume, a tradeoff that does not need to be considered with intrinsic approaches.

500

Being able to accurately sample curvature in 2-D across the hilltop-hillslope transition could also aid understanding of non-linear hillslope transport processes (Andrews and Bucknam, 1987; Roering et al., 1999). While this transition can be analyzed through 1-D profile analysis (Roering et al., 2007), this requires careful selection of hilltop profiles and limits the volume of land-surface information that can be utilized. The ability to accurately calculate surface curvature in 2-D and put this transition in a statistical, area-space framework could help connect 1-D models to densely sampled 2-D curvature values across complicated landscapes. It can also possibly simplify other approaches that leverage local coordinate systems to explore hillslope geometry (e.g. Bonetti et al. (2018)) by allowing for the use of the xy grid rather than other local coordinate vectors in calculating intrinsic metrics.

505

## 6.2 Comparison of tangent slope to 8-connected neighborhood gradient

510 Our approach to computing curvatures requires definition of a unit normal vector at every DEM grid cell, which also defines the slope of the local tangent plane ( $S_T$ ). We compare this method, which is mathematically equivalent to finding a slope magnitude using the Pythagorean sum of directional derivatives, to the commonly used 8-connected neighborhood gradient ( $D8$ ) that is the default in some landscape analysis toolboxes (Schwanghart and Scherler, 2014; Mudd et al., 2019). The  $D8$  method assigns a given pixel the slope between it and its lowest neighbor, providing an efficient flow routing algorithm (O’Callaghan and Mark, 1984). However, there are systematic deviations of this metric from true slopes at certain surface orientations. Figure 15.d shows the percent difference between the  $D8$  algorithm and true slope on the map-view projection of the unit sphere. Figure 15.e bins this deviation by azimuth (black line) and presents a comparison with both  $S_T$  on the sphere (blue dashed line), and the difference between  $S_t$  and  $D8$  on topography (cyan triangles).

515

Differences between  $D8$ -values and the analytic slope vary systematically with orientation of the surface up to magnitudes of  $\sim 7\%$ . The percent error in  $S_T$  on the sphere is near zero, while the differences between the various slope metrics on topography track the same azimuthal trend. This arises because the  $D8$ -algorithm tends to underestimate slope if pixels are miss-aligned with the direction of steepest descent. We bin the percent difference between  $S_T$  and  $D8$  by drainage area to track differences in the two metrics through the fluvial network (Fig. 15.f). The highest magnitude errors ( $\sim 35\%$ ) occur on ridges (Sect. 5.1.1), while the next highest magnitude negative errors ( $|\gt 20\%|$ ) occur at the highest drainage areas within the fluvial network (Sect. 5.1.4). Correlation with  $K_M$  (Fig 7) suggests sensitivity of the  $D8$ -algorithm to surface curvature as well as orientation.

520

525

## 6.3 Drainage surface area versus map-view area

As outlined in Sect. 3, this work is partially motivated by the fact that distances and areas on a sloped surface are greater than on their map-view representations. Specifically, the ratio of surface to pixel area can be calculated using the metric coefficients

as  $\alpha = \sqrt{EG - F}$ . To evaluate the effect of projection on drainage area values, we compute two separate area grids using the  
530 D-infinity flow routing algorithm in TopoToolbox (Schwanghart and Scherler, 2014), one with uniform pixel dimensions and  
another where pixels are weighted by  $\alpha$ . We bin the percent difference between these values by drainage area, with results  
shown in Fig. 15.f. Through most of the landscape, extrinsic drainage area calculations underestimate drainage surface area by  
10 – 15%.

There is an extensive literature on drainage area calculation, and drainage values are known to be sensitive to grid resolution  
535 (Bernard et al., 2022), filtering scale (Erdbrügger et al., 2021), and the choice of flow routing algorithm (Tarboton, 1997). It is  
beyond the scope of this study to systematically integrate our intrinsic approach with other sensitivities. We will simply point  
out that true land surface area is derivable from DEMs, and could be beneficial in some applications. For example, efforts  
to define drainage-scale hydrologic responses to snow melt in mountain basins depend on estimated snow water equivalent  
values interpolated over topography (Chen et al., 2022; Acharki et al., 2025); models that consider groundwater infiltration  
540 and soil carbon sequestration in addition to overland flow contain parameters that depend on land surface area (Taherian and  
Ameli, 2026; Hunter et al., 2024); and certain definitions of characteristic topographic length scales depend on measures of  
area accumulation defined on the surface (Gallant and Hutchinson, 2011; Grieve et al., 2016; Kargère et al., 2024). In each of  
these cases, the ability to accurately define surface area from map-view DEMs could be beneficial, though efforts to implement  
true surface area into process models has been shown to be inappropriate in some studies (e.g. Iverson and George (2024)).

## 545 7 Future directions

Quantitative classification of landforms and topography generally is challenged by the myriad interacting physical processes  
shaping landscapes at a range of spatial and temporal scales. Nevertheless, certain metrics such as local slope and drainage  
area have, through extensive empirical validation, proven to be useful indicators of spatial process transitions (Montgomery  
and Foufoula-Georgiou, 1993; Rosenbloom and Anderson, 1994; Stock and Dietrich, 2003) and transient landscape evolution  
550 (Kirby and Whipple, 2012; Royden and Perron, 2013).

While it is premature to claim that the curvature invariants used here have similar broad utility across landscapes, in our Coast  
Range study area these metrics – referenced to drainage area through  $\Sigma_G^j$  and  $\Sigma_M^j$  thresholds (Figs. 8-13) – separate the  
landscape into regimes that can be clearly associated with well known geomorphic processes. The  $\Sigma_G^j$  and  $\Sigma_M^j$  are separated  
by area-space inflection points (zero crossings) in Gaussian and mean curvature and appear to be minimally sensitive to DEM  
555 quality or smoothing. These  $\Sigma_i^j$  regimes, reflecting areas dominated by different combinations of convex and concave shape  
classes, should occur in all landscapes because they encode a distribution of ‘critical points’ that characterize stability and  
continuity in all 2D surfaces (Matsumoto, 2001; Goldsten et al., 2002; Bonetti et al., 2018). These geometries have implications  
for the sensitivity of landforms to external perturbation (Goldsten et al., 2002), and so we hypothesize that variation in drainage  
area values associated with  $\Sigma_i^j$  domains – perhaps in particular the concavity transition between  $\Sigma_M^0$  and  $\Sigma_M^1$  – may reflect  
560 signatures of landscape disequilibrium.

More broadly, the presence of persistent curvature patterns in structures of interest suggest the potential for new insights into geomorphic processes. For example, oscillations in principal curvatures within fluvial channels ( $\Sigma_G^3$  and Fig. 14) capture a step-pool morphology that is well documented in field studies (Grant et al., 1990; Montgomery and Buffington, 1997; Chartrand et al., 2011). This channel morphology is not explained by landscape evolution models that equate erosion rates to in-channel  
565 shear stress averaged over large spatio-temporal scales (Whipple and Tucker, 1999), but we show here that these oscillations are first order features of fluvial channel networks in the Oregon Coast Range. While the magnitude of these oscillations in curvature would need to be validated by field studies before any quantitative connections to process could be defined, the ability to potentially detect step-pool morphology at the landscape scale could open the door to connecting localized models of mass transport in rivers to landscape scale erosion models applied to topographic datasets (Venditti et al., 2020; Church and  
570 Zimmermann, 2007; Scheingross and Lamb, 2017; González et al., 2017; Escauriaza et al., 2023). In addition, the discernible valley widening signal discussed in Sect. 5.3 could aid understanding of known correlations between valley width and other landscape parameters (Bernard et al., 2022; Turowski et al., 2024).

Similarly, the ability to robustly identify colluvial hollows (a prominent component of  $\Sigma_G^2$ ), where the topographic surface is shaped by a superposition of competing processes at the onset of convergent topography (Dietrich et al., 1993), illustrates  
575 the power of this approach. In landscape regions shaped by debris flow processes (Struble et al., 2023), strongly disequilibrium dynamics (Donahue et al., 2013; Klema et al., 2023), glacial erosion (Kober et al., 2019), or even those dominated by constructional landforms such as in volcanic terrane (Karlstrom et al., 2025), slope-area scaling and other commonly used process-oriented classification approaches break down and tools such as developed here are likely to be useful. Because surface curvature also influences shallow subsurface stress state for rock fracture (Martel, 2011; Clair et al., 2015; Moon et al.,  
580 2017) and the hydraulic gradients driving groundwater flow (Wörman et al., 2006; Zhang et al., 2022), we expect that problems in Critical Zone science may also be examined through the lens of topographic curvature (Riebe et al., 2017).

Many processes driving landscape evolution have an intrinsic scale length (Wegmann et al., 2007; Crozier et al., 2018; Roering et al., 2010), so the combination of spectral filtering to isolate certain topographic features with curvature analysis seems a promising direction for future efforts in complex geomorphic settings (Perron et al., 2008; Struble et al., 2021). For example,  
585 1-D measures of hillslope length in the Oregon Coast Range (Grieve et al., 2016; Roering et al., 2007) could be compared to average path lengths in the  $\Sigma_G^1$  region to quantify similarities between intrinsic and extrinsic approaches, with a physically justified definition of the domain boundary given by our partitioning scheme. Quantitative comparison of our results with such studies of isolated landscape domains is a clear next step in development of these methods.

From a practical standpoint, Fig. 15.f highlights how intrinsic geometric computation of topographic metrics such as slope,  
590 curvature, and drainage area differ from the standard approach using an extrinsic map view projection of a DEM. The  $\Sigma_i^j$  regimes (e.g., as illustrated on Fig. 7.b) appear to be relevant. For example, curvature and drainage area computed over  $\Sigma_G^1$ , encompassing steep hillslopes, exhibit average differences of  $\sim 50\%$  and  $\sim 15\%$  respectively, which are larger than any other segment of the landscape. Slopes computed in either  $\Sigma_G^0$  or  $\Sigma_G^3$ , representing the smallest and largest drainage areas, are maximally different by  $\sim 30\%$ . Because the  $\Sigma_G^1$  region accounts for the majority of land surface area (Fig. 9.a), differences

595 in drainage area from  $\Sigma_G^1$  persist across all higher drainage areas with average values  $\sim 10\%$ . Understanding the effects of projection distortion on empirical scaling relations (e.g., Hack's Law, Hack et al. (1957), relies on drainage area computed from a DEM), and process-based models (e.g., sediment mass-continuity and stream power Whipple and Tucker (1999)), will likely be a fruitful direction for future work.

Perhaps the most exciting potential developments from this approach would be its application to high-resolution LiDAR data, where signatures of localized processes that drive landscape evolution can be better resolved (Roering et al., 2013). For example, it is known that hillslope processes are sensitive to bioturbation (Gabet, 2003), signatures of which cannot be resolved in the dataset used here. It is expected that the invariant approach to surface classification would be useful in resolving the topographic signatures of processes such as tree throw (Roering et al., 2010), which may heavily influence landscape-scale erosion. In the channel domain, this approach, when applied to LiDAR, could be useful in defining the geometry of complex channel features such as waterfall plunge pools (Scheingross and Lamb, 2017).

## 8 Conclusions

In this work we build a framework using the intrinsic surface characterization approach of Carl Frederick Gauss to derive topographic geometry metrics for landform characterization and landscape segmentation. By implementing tools of classical differential geometry to a landscape spectrally filtered to 200 m, we show how topography at a point can be categorized as one of four shape classes, providing a natural means of landscape segmentation that highlights channels, basins, domes, and saddles (28%, 22%, 23%, and 27% of the landscape respectively). We then show through an application to the Oregon Coast Range that the distribution of curvature invariants reveals details about the geometric evolution of fluvial systems that go beyond that captured by standard slope-area methods. We partition the area-space landscape into four domains based on the sign of the Gaussian curvature ( $\Sigma_G^0 - \Sigma_G^3$ ), and show how these partitions correspond to previously identified geomorphic process domains. Mapping mean curvature over the entire landscape reveals a remarkable symmetry that is reflected in total landscape curvature and slope distributions, and in the profile curvatures measured along ridge/channel networks. We hypothesize that such symmetry reflects a signature of steady-state fluvial topography. Lastly, we show that oscillations in curvatures perpendicular to channels and ridges is expressed in a regular geometric pattern that encode transitions in both concave and convex topography.

620 *Code and data availability.* The code used for data analysis is available at [https://github.com/ntklema/TopoCurve\\_Matlab](https://github.com/ntklema/TopoCurve_Matlab). The DEM data used in this study is available for download from The National Map at <https://apps.nationalmap.gov/downloader/>.

*Author contributions.* Conceptualization: NK, LK, Methodology: NK and LK, Visualization: NK and LK, Writing - original draft: NK, LK, and JR.

*Competing interests.* NK is a member of the editorial board of *Geomorphica*.

625 *Acknowledgements.* LK acknowledges support from NSF CAREER 1848554. LK acknowledges discussions with Jim Isenberg and with Ian Mynatt, who in different ways inspired interests in the differential geometry of geological surfaces. NK acknowledges that this work benefited from discussions with William Struble, Brooke Hunter, and Katharine Cashman.

## References

- Acharki, S., Boudhar, A., Bouihrouchane, A., Bousbaa, M., Karaoui, I., Elyoussfi, H., Bargam, B., Khalki, E. M. E., Hadri, A., and  
630 Chehbouni, A.: Spatial modeling of snow water equivalent in the high atlas mountains via a lumped process-based approach, *Scientific Reports*, 15, 26327, <https://doi.org/10.1038/s41598-025-12163-8>, 2025.
- Amundson, R., Heimsath, A., Owen, J., Yoo, K., and Dietrich, W. E.: Hillslope soils and vegetation, *Geomorphology*, 234, 122–132, <https://doi.org/10.1016/j.geomorph.2014.12.031>, 2015.
- Andrews, D. J. and Bucknam, R. C.: Fitting degradation of shoreline scarps by a nonlinear diffusion model, *Journal of Geophysical Research: Solid Earth*, 92, 12857–12867, <https://doi.org/10.1029/jb092ib12p12857>, 1987.  
635
- Baldwin, E. M.: Geologic map of the lower Umpqua River area, Oregon, Tech. rep., US Geological Survey, 1961.
- Bater, C. W. and Coops, N. C.: Evaluating error associated with lidar-derived DEM interpolation, *Computers and Geosciences*, 35, 289–300, <https://doi.org/10.1016/j.cageo.2008.09.001>, 2009.
- Beaulieu, J. D. and Hughes, P. W.: Environmental geology of western Coos and Douglas counties, Oregon, Tech. rep., State of Oregon,  
640 Department of Geology and Mineral Industries, 1975.
- Bergbauer, S. and Pollard, D. D.: How to calculate normal curvatures of sampled geological surfaces, *Journal of Structural Geology*, 25, 277–289, [https://doi.org/10.1016/s0191-8141\(02\)00019-6](https://doi.org/10.1016/s0191-8141(02)00019-6), 2003.
- Bernard, T. G., Davy, P., and Lague, D.: Hydro-Geomorphic Metrics for High Resolution Fluvial Landscape Analysis, *Journal of Geophysical Research: Earth Surface*, 127, <https://doi.org/10.1029/2021jf006535>, 2022.
- 645 Black, B. A., Perron, J. T., Hemingway, D., Bailey, E., Nimmo, F., and Zebker, H.: Planetary topography: Global drainage patterns and the origins of topographic relief on Earth, Mars, and Titan, *Science*, 356, 727–731, <https://doi.org/10.1126/science.aag0171>, 2017.
- Bonetti, S., Bragg, A. D., and Porporato, A.: On the theory of drainage area for regular and non-regular points, *Proceedings of the Royal Society A: Mathematical, Physical and Engineering Sciences*, 474, 20170693, <https://doi.org/10.1098/rspa.2017.0693>, 2018.
- Bonetti, S., Hooshyar, M., Camporeale, C., and Porporato, A.: Channelization cascade in landscape evolution, *Proceedings of the National Academy of Sciences*, 117, 1375–1382, <https://doi.org/10.1073/pnas.1911817117>, 2020.  
650
- Booth, A. M., Roering, J. J., and Perron, J. T.: Automated landslide mapping using spectral analysis and high-resolution topographic data: Puget Sound lowlands, Washington, and Portland Hills, Oregon, *Geomorphology*, 109, 132–147, <https://doi.org/10.1016/j.geomorph.2009.02.027>, 2009.
- Brigham, C. A. and Crider, J. G.: A new metric for morphologic variability using landform shape classification via supervised machine  
655 learning, *Geomorphology*, 399, 108065, <https://doi.org/10.1016/j.geomorph.2021.108065>, 2022.
- Bui, L. K. and Glennie, C. L.: Estimation of lidar-based gridded DEM uncertainty with varying terrain roughness and point density, *ISPRS Open Journal of Photogrammetry and Remote Sensing*, 7, 100028, <https://doi.org/10.1016/j.ophoto.2022.100028>, 2023.
- Cayley: XL. On contour and slope lines, *The London, Edinburgh, and Dublin Philosophical Magazine and Journal of Science*, 18, 264–268, <https://doi.org/10.1080/14786445908642760>, 1859.
- 660 Chartrand, S. M., Jellinek, M., Whiting, P. J., and Stamm, J.: Geometric scaling of step-pools in mountain streams: Observations and implications, *Geomorphology*, 129, 141–151, <https://doi.org/10.1016/j.geomorph.2011.01.020>, 2011.
- Chen, X., Tang, G., Chen, T., and Niu, X.: An Assessment of the Impacts of Snowmelt Rate and Continuity Shifts on Streamflow Dynamics in Three Alpine Watersheds in the Western U.S., *Water*, 14, 1095, <https://doi.org/10.3390/w14071095>, 2022.
- Church, M. and Zimmermann, A.: Form and stability of step-pool channels: Research progress, *Water Resources Research*, 43, 1–21,  
665 <https://doi.org/10.1029/2006wr005037>, 2007.

- Clair, J. S., Moon, S., Holbrook, W. S., Perron, J. T., Riebe, C. S., Martel, S. J., Carr, B., Harman, C., Singha, K., and Richter, D. d.: Geophysical imaging reveals topographic stress control of bedrock weathering, *Science*, 350, 534–538, <https://doi.org/10.1126/science.aab2210>, 2015.
- 670 Crosby, C. J., Arrowsmith, J. R., and Nandigam, V.: Chapter 11 Zero to a trillion: Advancing Earth surface process studies with open access to high-resolution topography, *Developments in Earth Surface Processes*, 23, 317–338, <https://doi.org/10.1016/b978-0-444-64177-9.00011-4>, 2020.
- Crozier, J., Karlstrom, L., and Yang, K.: Basal control of supraglacial meltwater catchments on the Greenland Ice Sheet, *The Cryosphere*, 12, 3383–3407, <https://doi.org/10.5194/tc-12-3383-2018>, 2018.
- Culling, W. E. H.: Analytical Theory of Erosion, *The Journal of Geology*, 68, 336–344, <https://doi.org/10.1086/626663>, 1960.
- 675 Daly, C. and Bryant, K.: *The PRISM Climate and Weather System – An Introduction*, Corvallis, OR: PRISM climate group 2, 2013.
- Davis, A. W. M.: The Convex Profile of Bad-Land Divides, *Science*, 20, 27–28, 1892.
- Deshpande, N. S., Furbish, D. J., Arratia, P. E., and Jerolmack, D. J.: The perpetual fragility of creeping hillslopes, *Nature Communications*, 12, 3909, <https://doi.org/10.1038/s41467-021-23979-z>, 2021.
- Dietrich, W. E. and Dunne, T.: *Sediment budget for a small catchment in a mountainous terrain*, Routledge: London, UK, 1978.
- 680 Dietrich, W. E., Wilson, C. J., Montgomery, D. R., and McKean, J.: Analysis of Erosion Thresholds, Channel Networks, and Landscape Morphology Using a Digital Terrain Model, *The Journal of Geology*, 101, 259–278, <https://doi.org/10.1086/648220>, 1993.
- Donahue, M. S., Karlstrom, K. E., Aslan, A., Darling, A., Granger, D., Wan, E., Dickinson, R. G., and Kirby, E.: Incision history of the Black Canyon of Gunnison, Colorado, over the past ~ 1 Ma inferred from dating of fluvial gravel deposits, *Geosphere*, 9, 815–826, <https://doi.org/10.1130/ges00847.1>, 2013.
- 685 Erdbrügger, J., Meerveld, I. v., Bishop, K., and Seibert, J.: Effect of DEM-smoothing and -aggregation on topographically-based flow directions and catchment boundaries, *Journal of Hydrology*, 602, 126 717, <https://doi.org/10.1016/j.jhydrol.2021.126717>, 2021.
- Escauriaza, C., González, C., Williams, M. E., and Brevis, W.: Models of bed-load transport across scales: turbulence signature from grain motion to sediment flux, *Stochastic Environmental Research and Risk Assessment*, 37, 1039–1052, <https://doi.org/10.1007/s00477-022-02333-9>, 2023.
- 690 Fenneman, N.: Some Features of Erosion by Unconcentrated Wash, *The Journal of Geology*, 16, 746–754, 1908.
- Fernandes, N. F. and Dietrich, W. E.: Hillslope evolution by diffusive processes: The timescale for equilibrium adjustments, *Water Resources Research*, 33, 1307–1318, <https://doi.org/10.1029/97wr00534>, 1997.
- Ferrier, K. L., Huppert, K. L., and Perron, J. T.: Climatic control of bedrock river incision, *Nature*, 496, 206–209, <https://doi.org/10.1038/nature11982>, 2013.
- 695 Flint, J. J.: Stream gradient as a function of order, magnitude, and discharge, *Water Resources Research*, 10, 969–973, <https://doi.org/10.1029/wr010i005p00969>, 1974.
- Furbish, D. J., Haff, P. K., Dietrich, W. E., and Heimsath, A. M.: Statistical description of slope-dependent soil transport and the diffusion-like coefficient, *Journal of Geophysical Research: Earth Surface*, 114, <https://doi.org/10.1029/2009jf001267>, 2009.
- Gabet, E. J.: Sediment transport by dry ravel, *Journal of Geophysical Research: Solid Earth*, 108, <https://doi.org/10.1029/2001jb001686>, 700 2003.
- Gallant, J.: Adaptive smoothing for noisy DEMs, *Geomorphometry*, 2011, 7–9, 2011.
- Gallant, J. C. and Hutchinson, M. F.: A differential equation for specific catchment area, *Water Resources Research*, 47, <https://doi.org/10.1029/2009wr008540>, 2011.

- Gauss, C. F.: General Investigations of Curved Surfaces of 1827 and 1825, *Nature*, 66, 316–317, <https://doi.org/10.1038/066316b0>, 1902.
- 705 Gilbert, G. K.: *Geology of the Henry Mountains*, U.S. Geographical and Geological Survey of the Rocky Mountain Region, p. 196, 1877.
- Goldsten, H., Safko, J., and Poole, C.: *Classical Mechanics*, Addison-Wesley, 3rd edn., 2002.
- González, C., Richter, D. H., Bolster, D., Bateman, S., Calantoni, J., and Escauriaza, C.: Characterization of bedload intermittency near the threshold of motion using a Lagrangian sediment transport model, *Environmental Fluid Mechanics*, 17, 111–137, <https://doi.org/10.1007/s10652-016-9476-x>, 2017.
- 710 Grant, G. E., Swanson, F. J., and Wolman, M. G.: Pattern and origin of stepped-bed morphology in high-gradient streams, Western Cascades, Oregon, *GSA Bulletin*, 102, 340–352, [https://doi.org/10.1130/0016-7606\(1990\)102<0340:paoosb>2.3.co;2](https://doi.org/10.1130/0016-7606(1990)102<0340:paoosb>2.3.co;2), 1990.
- Grieve, S. W., Mudd, S. M., and Hurst, M. D.: How long is a hillslope?, *Earth Surface Processes and Landforms*, 41, 1039–1054, <https://doi.org/10.1002/esp.3884>, 2016.
- Hack, J. T., Seaton, F. A., and Nolan, T. B.: *Studies of Longitudinal Stream Profiles in Virginia and Maryland*, vol. 294, US Government Printing Office, 1957.
- 715 Harris, F. J.: On the Use of Windows for Harmonic Analysis with the Discrete Fourier Transform, *Proceedings of the IEEE*, 66, 51–83, <https://doi.org/10.1109/proc.1978.10837>, 1978.
- Heideman, M. T., Johnson, D. H., and Burrus, C. S.: Gauss and the history of the fast Fourier transform, *Archive for History of Exact Sciences*, 34, 265–277, <https://doi.org/10.1007/bf00348431>, 1985.
- 720 Heimsath, A. M., Dietrich, W. E., Nishiizumi, K., and Finkel, R. C.: Stochastic processes of soil production and transport: erosion rates, topographic variation and cosmogenic nuclides in the Oregon Coast Range, *Earth Surface Processes and Landforms*, 26, 531–552, <https://doi.org/10.1002/esp.209>, 2001.
- Hooshyar, M., Bonetti, S., Singh, A., Foufoula-Georgiou, E., and Porporato, A.: From turbulence to landscapes: Logarithmic mean profiles in bounded complex systems, *Physical Review E*, 102, 033 107, <https://doi.org/10.1103/physreve.102.033107>, 2020.
- 725 Hunter, B. D., Roering, J. J., Silva, L. C. R., and Moreland, K. C.: Geomorphic controls on the abundance and persistence of soil organic carbon pools in erosional landscapes, *Nature Geoscience*, 17, 151–157, <https://doi.org/10.1038/s41561-023-01365-2>, 2024.
- Hurst, M. D., Mudd, S. M., Walcott, R., Attal, M., and Yoo, K.: Using hilltop curvature to derive the spatial distribution of erosion rates, *Journal of Geophysical Research: Earth Surface*, 117, <https://doi.org/10.1029/2011jf002057>, 2012.
- Iverson, R. M. and George, D. L.: *Advances in Debris-flow Science and Practice*, *Geoenvironmental Disaster Reduction*, pp. 127–163, 730 [https://doi.org/10.1007/978-3-031-48691-3\\_5](https://doi.org/10.1007/978-3-031-48691-3_5), 2024.
- Jaeger, H. M. and Nagel, S. R.: *Physics of the Granular State*, *Science*, 255, 1523–1531, <https://doi.org/10.1126/science.255.5051.1523>, 1992.
- Jasiewicz, J. and Stepinski, T. F.: Geomorphons — a pattern recognition approach to classification and mapping of landforms, *Geomorphology*, 182, 147–156, <https://doi.org/10.1016/j.geomorph.2012.11.005>, 2013.
- 735 Jordan, G.: Adaptive smoothing of valleys in DEMs using TIN interpolation from ridgeline elevations: An application to morphotectonic aspect analysis, *Computers & Geosciences*, 33, 573–585, <https://doi.org/10.1016/j.cageo.2006.08.010>, 2007.
- Kargère, B. A., Constantine, J. A., Hales, T. C., Grieve, S. W. D., and Johnson, S. D.: A Fractal Framework for Channel-Hillslope Coupling, *EGUsphere*, 2024, 1–24, <https://doi.org/10.5194/egusphere-2024-2847>, 2024.
- Karlstrom, L., Klema, N., Grant, G. E., Finn, C., Sullivan, P. L., Cooley, S., Simpson, A., Fasth, B., Cashman, K., Ferrier, K., Ball, L., and 740 McKay, D.: State shifts in the deep Critical Zone drive landscape evolution in volcanic terrains, *Proceedings of the National Academy of Sciences*, 122, e2415155 122, <https://doi.org/10.1073/pnas.2415155122>, 2025.

- Kelsey, H. M., Ticknor, R. L., Bockheim, J. G., and Mitchell, E.: Quaternary upper plate deformation in coastal Oregon, *GSA Bulletin*, 108, 843–860, [https://doi.org/10.1130/0016-7606\(1996\)108<0843:qupdic>2.3.co;2](https://doi.org/10.1130/0016-7606(1996)108<0843:qupdic>2.3.co;2), 1996.
- Kirby, E. and Whipple, K. X.: Expression of active tectonics in erosional landscapes, *Journal of Structural Geology*, 44, 54–75, <https://doi.org/10.1016/j.jsg.2012.07.009>, 2012.
- 745
- Klema, N., Karlstrom, L., Cannon, C., Jiang, C., O'Connor, J., Wells, R., and Schmandt, B.: The magmatic origin of the Columbia River Gorge, USA, *Science Advances*, 9, eadj3357, <https://doi.org/10.1126/sciadv.adj3357>, 2023.
- Kober, F., Hippe, K., Salcher, B., Grischott, R., Zurfluh, R., Hajdas, I., Wacker, L., Christl, M., and Ivy-Ochs, S.: Postglacial to Holocene landscape evolution and process rates in steep alpine catchments, *Earth Surface Processes and Landforms*, 44, 242–258, <https://doi.org/10.1002/esp.4491>, 2019.
- 750
- LaHusen, S. R., Duvall, A. R., Booth, A. M., Grant, A., Mishkin, B. A., Montgomery, D. R., Struble, W., Roering, J. J., and Wartman, J.: Rainfall triggers more deep-seated landslides than Cascadia earthquakes in the Oregon Coast Range, USA, *Science Advances*, 6, eaba6790, <https://doi.org/10.1126/sciadv.aba6790>, 2020.
- Luu, C., Forino, G., Yorke, L., Ha, H., Bui, Q. D., Tran, H. H., Nguyen, D. Q., Duong, H. C., and Kervyn, M.: Integrating susceptibility maps of multiple hazards and building exposure distribution: a case study of wildfires and floods for the province of Quang Nam, Vietnam, *Natural Hazards and Earth System Sciences*, 24, 4385–4408, <https://doi.org/10.5194/nhess-24-4385-2024>, 2024.
- 755
- Martel, S. J.: Mechanics of curved surfaces, with application to surface-parallel cracks, *Geophysical Research Letters*, 38, n/a–n/a, <https://doi.org/10.1029/2011gl049354>, 2011.
- Matsumoto, Y.: An Introduction to Morse Theory, *Translations of Mathematical Monographs*, pp. 33–72, <https://doi.org/10.1090/mmono/208/02>, 2001.
- 760
- Maxwell, J. C.: L. on hills and dales: To the editors of the philosophical magazine and journal, *The London, Edinburgh, and Dublin Philosophical Magazine and Journal of Science*, 40, 421–427, <https://doi.org/10.1080/14786447008640422>, 1870.
- Mcguire, L. A., Mccoy, S. W., Marc, O., Struble, W., and Barnhart, K. R.: Steady-state forms of channel profiles shaped by debris-flow and fluvial processes, *Earth Surface Dynamics Discussions*, pp. 1–33, <https://doi.org/10.5194/esurf-2022-47>, 2022.
- 765
- McNeill, L. C., Goldfinger, C., Kulm, L. D., and Yeats, R. S.: Tectonics of the Neogene Cascadia forearc basin: Investigations of a deformed late Miocene unconformity, *GSA Bulletin*, 112, 1209–1224, [https://doi.org/10.1130/0016-7606\(2000\)112<1209:totnfc>2.0.co;2](https://doi.org/10.1130/0016-7606(2000)112<1209:totnfc>2.0.co;2), 2000.
- McNutt, M.: Influence Of Plate Subduction On Isostatic Compensation in Northern California, *Tectonics*, 4, 399–415, 1983.
- Minár, J., Evans, I. S., and Jenčo, M.: A comprehensive system of definitions of land surface (topographic) curvatures, with implications for their application in geoscience modelling and prediction, *Earth-Science Reviews*, 211, 103414, <https://doi.org/10.1016/j.earscirev.2020.103414>, 2020.
- 770
- Montgomery, D. R.: Slope Distributions, Threshold Hillslopes, and Steady-state Topography, *American Journal of Science*, 301, 432–454, <https://doi.org/10.2475/ajs.301.4-5.432>, 2001.
- Montgomery, D. R. and Buffington, J. M.: Channel-reach morphology in mountain drainage basins, *GSA Bulletin*, 109, 596–611, [https://doi.org/10.1130/0016-7606\(1997\)109<0596:crmimd>2.3.co;2](https://doi.org/10.1130/0016-7606(1997)109<0596:crmimd>2.3.co;2), 1997.
- 775
- Montgomery, D. R. and Foufoula-Georgiou, E.: Channel network source representation using digital elevation models, *Water Resources Research*, 29, 3925–3934, <https://doi.org/10.1029/93wr02463>, 1993.
- Moon, S., Perron, J. T., Martel, S. J., Holbrook, W. S., and Clair, J. S.: A model of three-dimensional topographic stresses with implications for bedrock fractures, surface processes, and landscape evolution, *Journal of Geophysical Research: Earth Surface*, 122, 823–846, <https://doi.org/10.1002/2016jf004155>, 2017.

- 780 Mudd, S. M., Gailleton, B., Clubb, F., Grieve, S., and Valters, D.: LSDTopoTools2 v2.01 (Version v2.01), <http://doi.org/10.5281/zenodo.3245076>, 2019.
- Mynatt, I., Bergbauer, S., and Pollard, D. D.: Using differential geometry to describe 3-D folds, *Journal of Structural Geology*, 29, 1256–1266, <https://doi.org/10.1016/j.jsg.2007.02.006>, 2007.
- Needham, T.: *Visual Differential Geometry and Forms: A Mathematical Drama in Five Acts*, Princeton University Press, Princeton, 2021.
- 785 O’Callaghan, J. F. and Mark, D. M.: The extraction of drainage networks from digital elevation data, *Computer Vision, Graphics, and Image Processing*, 28, 323–344, [https://doi.org/10.1016/s0734-189x\(84\)80011-0](https://doi.org/10.1016/s0734-189x(84)80011-0), 1984.
- O’Hara, D., Karlstrom, L., and Roering, J. J.: Distributed landscape response to localized uplift and the fragility of steady states, *Earth and Planetary Science Letters*, 506, 243–254, <https://doi.org/10.1016/j.epsl.2018.11.006>, 2019.
- O’Neill, B.: *Elementary differential geometry*, Elementary differential geometry, 2006.
- 790 Osserman, R.: *A survey of minimal surfaces*, Courier Corporation, 2013.
- Passalacqua, P., Trung, T. D., Fouloula-Georgiou, E., Sapiro, G., and Dietrich, W. E.: A geometric framework for channel network extraction from lidar: Nonlinear diffusion and geodesic paths, *Journal of Geophysical Research: Earth Surface*, 115, <https://doi.org/10.1029/2009jg001254>, 2010.
- Pearce, M. A., Jones, R. R., Smith, S. A., McCaffrey, K. J., and Clegg, P.: Numerical analysis of fold curvature using data acquired by high-precision GPS, *Journal of Structural Geology*, 28, 1640–1646, <https://doi.org/10.1016/j.jsg.2006.05.010>, 2006.
- 795 Perron, J. T., Kirchner, J. W., and Dietrich, W. E.: Spectral signatures of characteristic spatial scales and nonfractal structure in landscapes, *Journal of Geophysical Research: Earth Surface*, 113, <https://doi.org/10.1029/2007jg000866>, 2008.
- Perron, J. T., Kirchner, J. W., and Dietrich, W. E.: Formation of evenly spaced ridges and valleys, *Nature*, 460, 502–505, <https://doi.org/10.1038/nature08174>, 2009.
- 800 Perron, J. T., Richardson, P. W., Ferrier, K. L., and Lapôtre, M.: The root of branching river networks, *Nature*, 492, 100–103, <https://doi.org/10.1038/nature11672>, 2012.
- Personius, S. F.: Late Quaternary stream incision and uplift in the forearc of the Cascadia subduction zone, western Oregon, *Journal of Geophysical Research: Solid Earth*, 100, 20 193–20 210, <https://doi.org/10.1029/95jb01684>, 1995.
- Pesic, P.: *Beyond Geometry: Classic Papers from Riemann to Einstein*, Courier Corporation, 2007.
- 805 Reneau, S. L. and Dietrich, W. E.: Erosion rates in the southern oregon coast range: Evidence for an equilibrium between hillslope erosion and sediment yield, *Earth Surface Processes and Landforms*, 16, 307–322, <https://doi.org/10.1002/esp.3290160405>, 1991.
- Reuter, H. I., Hengl, T., Gessler, P., and Soille, P.: Preparation of DEMs for geomorphometric analysis, *Developments in Soil Science*, 33, 87–120, [https://doi.org/10.1016/s0166-2481\(08\)00004-4](https://doi.org/10.1016/s0166-2481(08)00004-4), 2009.
- Richardson, P. and Karlstrom, L.: The multi-scale influence of topography on lava flow morphology, *Bulletin of Volcanology*, 81, 21, <https://doi.org/10.1007/s00445-019-1278-9>, 2019.
- 810 Riebe, C. S., Hahm, W. J., and Brantley, S. L.: Controls on deep critical zone architecture: a historical review and four testable hypotheses, *Earth Surface Processes and Landforms*, 42, 128–156, <https://doi.org/10.1002/esp.4052>, 2017.
- Riza, S., Sekine, M., Kanno, A., Yamamoto, K., Imai, T., and Higuchi, T.: Land Suitability Analysis for Agricultural Land Use using Hyperscale DEM Data, *AGRIVITA Journal of Agricultural Science*, 44, <https://doi.org/10.17503/agrivita.v44i2.2985>, 2022.
- 815 Roering, J. J., Kirchner, J. W., and Dietrich, W. E.: Evidence for nonlinear, diffusive sediment transport on hillslopes and implications for landscape morphology, *Water Resources Research*, 35, 853–870, <https://doi.org/10.1029/1998wr900090>, 1999.

- Roering, J. J., Kirchner, J. W., and Dietrich, W. E.: Hillslope evolution by nonlinear, slope-dependent transport: Steady state morphology and equilibrium adjustment timescales, *Journal of Geophysical Research: Solid Earth*, 106, 16499–16513, <https://doi.org/10.1029/2001jb000323>, 2001a.
- 820 Roering, J. J., Kirchner, J. W., Sklar, L. S., and Dietrich, W. E.: Hillslope evolution by nonlinear creep and landsliding: An experimental study, *Geology*, 29, 143–146, [https://doi.org/10.1130/0091-7613\(2001\)029<0143:hebnca>2.0.co;2](https://doi.org/10.1130/0091-7613(2001)029<0143:hebnca>2.0.co;2), 2001b.
- Roering, J. J., Kirchner, J. W., and Dietrich, W. E.: Characterizing structural and lithologic controls on deep-seated landsliding: Implications for topographic relief and landscape evolution in the Oregon Coast Range, USA, *Bulletin of the Geological Society of America*, 117, 654–668, <https://doi.org/10.1130/b25567.1>, 2005.
- 825 Roering, J. J., Perron, J. T., and Kirchner, J. W.: Functional relationships between denudation and hillslope form and relief, *Earth and Planetary Science Letters*, 264, 245–258, <https://doi.org/10.1016/j.epsl.2007.09.035>, 2007.
- Roering, J. J., Marshall, J., Booth, A. M., Mort, M., and Jin, Q.: Evidence for biotic controls on topography and soil production, *Earth and Planetary Science Letters*, 298, 183–190, <https://doi.org/10.1016/j.epsl.2010.07.040>, 2010.
- Roering, J. J., Mackey, B. H., Marshall, J. A., Sweeney, K. E., Deligne, N. I., Booth, A. M., Handwerger, A. L., and Cerovski-Darriau, C.: ‘You are HERE’: Connecting the dots with airborne lidar for geomorphic fieldwork, *Geomorphology*, 200, 172–183, <https://doi.org/10.1016/j.geomorph.2013.04.009>, 2013.
- 830 Rosenbloom, N. A. and Anderson, R. S.: Hillslope and channel evolution in a marine terraced landscape, Santa Cruz, California, *Journal of Geophysical Research: Solid Earth*, 99, 14 013–14 029, <https://doi.org/10.1029/94jb00048>, 1994.
- Royden, L. and Perron, J. T.: Solutions of the stream power equation and application to the evolution of river longitudinal profiles, *Journal of Geophysical Research: Earth Surface*, 118, 497–518, <https://doi.org/10.1002/jgrf.20031>, 2013.
- 835 Ruh, J. B.: Numerical modeling of tectonic underplating in accretionary wedge systems, *Geosphere*, 16, 1385–1407, <https://doi.org/10.1130/ges02273.1>, 2020.
- Scheingross, J. S. and Lamb, M. P.: A Mechanistic Model of Waterfall Plunge Pool Erosion into Bedrock, *Journal of Geophysical Research: Earth Surface*, 122, 2079–2104, <https://doi.org/10.1002/2017jf004195>, 2017.
- 840 Scherler, D. and Schwanghart, W.: Identification and ordering of drainage divides in digital elevation models, *Earth Surface Dynamics Discussions*, pp. 1–35, <https://doi.org/10.5194/esurf-2019-51>, 2019.
- Schmidt, J., Evans, I. S., and Brinkmann, J.: Comparison of polynomial models for land surface curvature calculation, *International Journal of Geographical Information Science*, 17, 797–814, <https://doi.org/10.1080/13658810310001596058>, 2003.
- Schwanghart, W. and Scherler, D.: Short Communication: TopoToolbox 2 – MATLAB-based software for topographic analysis and modeling in Earth surface sciences, *Earth Surface Dynamics*, 2, 1–7, <https://doi.org/10.5194/esurf-2-1-2014>, 2014.
- 845 Shary, P. A.: Land surface in gravity points classification by a complete system of curvatures, *Mathematical Geology*, 27, 373–390, <https://doi.org/10.1007/bf02084608>, 1995.
- Sofia, G.: Combining geomorphometry, feature extraction techniques and Earth-surface processes research: The way forward, *Geomorphology*, 355, 107 055, <https://doi.org/10.1016/j.geomorph.2020.107055>, 2020.
- 850 Stewart, J.: *Multivariable Calculus*, Brooks Cole, 2003.
- Stock, J. and Dietrich, W. E.: Valley incision by debris flows: Evidence of a topographic signature, *Water Resources Research*, 39, <https://doi.org/10.1029/2001wr001057>, 2003.
- Stock, J. D. and Montgomery, D. R.: Geologic constraints on bedrock river incision using the stream power law, *Journal of Geophysical Research: Solid Earth*, 104, 4983–4993, <https://doi.org/10.1029/98jb02139>, 1999.

- 855 Struble, W. T., Roering, J. J., Dorsey, R. J., and Bendick, R.: Characteristic Scales of Drainage Reorganization in Cascadia, *Geophysical Research Letters*, 48, <https://doi.org/10.1029/2020gl091413>, 2021.
- Struble, W. T., McGuire, L. A., McCoy, S. W., Barnhart, K. R., and Marc, O.: Debris-Flow Process Controls on Steepland Morphology in the San Gabriel Mountains, California, *Journal of Geophysical Research: Earth Surface*, 128, <https://doi.org/10.1029/2022jf007017>, 2023.
- Struble, W. T., Clubb, F. J., and Roering, J. J.: Regional-scale, high-resolution measurements of hilltop curvature reveal  
860 tectonic, climatic, and lithologic controls on hillslope morphology, *Earth and Planetary Science Letters*, 647, 119 044, <https://doi.org/10.1016/j.epsl.2024.119044>, 2024.
- Struik, D. J. D. J.: *Lectures on classical differential geometry*, Lectures on classical differential geometry, 1950.
- Taherian, M. and Ameli, A. A.: Time Variance in Snowmelt Partitioning: A Mechanistic Modeling Approach to Explore the Role of Catchment Structure and Pre-Snow Rainfall, *Water Resources Research*, 62, <https://doi.org/10.1029/2025wr040679>, 2026.
- 865 Tarboton, D. G.: A new method for the determination of flow directions and upslope areas in grid digital elevation models, *Water Resources Research*, 33, 309–319, <https://doi.org/10.1029/96wr03137>, 1997.
- Tucker, G. E., Lancaster, S. T., Gasparini, N. M., Bras, R. L., and Rybarczyk, S. M.: An object-oriented framework for distributed hydrologic and geomorphic modeling using triangulated irregular networks, *Computers & Geosciences*, 27, 959–973, [https://doi.org/10.1016/s0098-3004\(00\)00134-5](https://doi.org/10.1016/s0098-3004(00)00134-5), 2001.
- 870 Turcotte, D. L.: A fractal interpretation of topography and geoid spectra on the Earth, Moon, Venus, and Mars, *Journal of Geophysical Research: Solid Earth*, 92, E597–E601, <https://doi.org/10.1029/jb092ib04p0e597>, 1987.
- Turowski, J. M., Bufer, A., and Tofelde, S.: A physics-based model for fluvial valley width, *Earth Surface Dynamics*, 12, 493–514, <https://doi.org/10.5194/esurf-12-493-2024>, 2024.
- Venditti, J. G., Li, T., Deal, E., Dingle, E., and Church, M.: Struggles with stream power: Connecting theory across scales, *Geomorphology*,  
875 366, 106 817, <https://doi.org/10.1016/j.geomorph.2019.07.004>, 2020.
- Watts, A. B.: *Isostasy and flexure of the lithosphere*, Cambridge University Press, Cambridge, United Kingdom, 2001.
- Wegmann, K. W., Zurek, B. D., Regalla, C. A., Bilardello, D., Wollenberg, J. L., Kopczynski, S. E., Ziemann, J. M., Haight, S. L., Apgar, J. D., Zhao, C., and Pazzaglia, F. J.: Position of the Snake River watershed divide as an indicator of geodynamic processes in the greater Yellowstone region, western North America, *Geosphere*, 3, 272–281, <https://doi.org/10.1130/ges00083.1>, 2007.
- 880 Wells, R., Bukry, D., Friedman, R., Pyle, D., Duncan, R., Haeussler, P., and Wooden, J.: Geologic history of Siletzia, a large igneous province in the Oregon and Washington Coast Range: Correlation to the geomagnetic polarity time scale and implications for a long-lived Yellowstone hotspot, *Geosphere*, 10, 692–719, <https://doi.org/10.1130/ges01018.1>, 2014.
- Whipple, K., DiBiase, R., and Crosby, B.: *Treatise on Geomorphology, Specific Fluvial Environments*, pp. 550–573, <https://doi.org/10.1016/b978-0-12-374739-6.00254-2>, 2013.
- 885 Whipple, K. X. and Tucker, G. E.: Dynamics of the stream-power river incision model: Implications for height limits of mountain ranges, landscape response timescales, and research needs, *Journal of Geophysical Research: Solid Earth*, 104, 17 661–17 674, <https://doi.org/10.1029/1999jb900120>, 1999.
- Wieczorek, M. A.: *Gravity and Topography of the Terrestrial Planets*, *Treatise on geophysics*, 10, 165–206, <https://doi.org/10.1016/b978-0-444-53802-4.00169-x>, 2015.
- 890 Willett, S. D.: Erosion on a line, *Tectonophysics*, 484, 168–180, <https://doi.org/10.1016/j.tecto.2009.09.011>, 2010.

- Wobus, C., Whipple, K. X., Kirby, E., Snyder, N., Johnson, J., Spyropolou, K., Crosby, B., and Sheehan, D.: Tectonics from topography: Procedures, promise, and pitfalls, *Special Paper of the Geological Society of America*, 398, 55–74, [https://doi.org/10.1130/2006.2398\(04\)](https://doi.org/10.1130/2006.2398(04)), 2006.
- 895 Wörman, A., Packman, A. I., Marklund, L., Harvey, J. W., and Stone, S. H.: Exact three-dimensional spectral solution to surface-groundwater interactions with arbitrary surface topography, *Geophysical Research Letters*, 33, <https://doi.org/10.1029/2006gl025747>, 2006.
- Yanites, B. J., Clark, M. K., Roering, J. J., West, A. J., Zekkos, D., Baldwin, J. W., Cerovski-Darriau, C., Gallen, S. F., Horton, D. E., Kirby, E., Leshchinsky, B. A., Mason, H. B., Moon, S., Barnhart, K. R., Booth, A., Czuba, J. A., McCoy, S., McGuire, L., Pfeiffer, A., and Pierce, J.: Cascading land surface hazards as a nexus in the Earth system, *Science*, 388, eadp9559, <https://doi.org/10.1126/science.adp9559>, 2025.
- 900 Zhang, X., Jiao, J. J., and Guo, W.: How Does Topography Control Topography-Driven Groundwater Flow?, *Geophysical Research Letters*, 49, <https://doi.org/10.1029/2022gl101005>, 2022.